

JGR Solid Earth

RESEARCH ARTICLE

10.1029/2025JB031674

Key Points:

- We observed amplitude-dependent attenuation of polycrystalline olivine during forced-oscillation experiments in the deformation-DIA
- Our results support the backstress mechanism for the transient behavior of the upper mantle in lieu of intergranular mechanisms
- The backstress model acts linear viscoelastic at small amplitudes and may explain the strength of seismic attenuation in the upper mantle

Supporting Information:

Supporting Information may be found in the online version of this article.

Correspondence to:

D. Hein,
hein0477@umn.edu

Citation:

Hein, D., Hansen, L. N., Kumamoto, K. M., Chen, H., Nehring, M. A., Goddard, R. M., et al. (2025). The role of dislocations in the anelasticity of the upper mantle. *Journal of Geophysical Research: Solid Earth*, 130, e2025JB031674. <https://doi.org/10.1029/2025JB031674>

Received 26 MAR 2025

Accepted 12 SEP 2025

Author Contributions:

Conceptualization: Diède Hein, Lars N. Hansen, Thomas Breithaupt

Data curation: Diède Hein

Formal analysis: Diède Hein

Funding acquisition: Lars N. Hansen

Investigation: Diède Hein, Lars N. Hansen, Kathryn M. Kumamoto, Haiyan Chen, M. Adaire Nehring, Rellie M. Goddard, Thomas Breithaupt, Andrew J. Cross, Christopher A. Thom, Caroline Seyler

Methodology: Diède Hein, Kathryn M. Kumamoto, Haiyan Chen

Project administration: Lars N. Hansen

Resources: Diède Hein, Kathryn M. Kumamoto, Haiyan Chen, M. Adaire Nehring, Rellie M. Goddard

Supervision: Lars N. Hansen, Kathryn M. Kumamoto, Haiyan Chen, M. Adaire Nehring, Rellie M. Goddard

Validation: Diède Hein, Kathryn M. Kumamoto, Haiyan Chen, M. Adaire Nehring, Rellie M. Goddard

Visualization: Diède Hein, Kathryn M. Kumamoto, Haiyan Chen, M. Adaire Nehring, Rellie M. Goddard

Writing—original draft: Diède Hein, Kathryn M. Kumamoto, Haiyan Chen, M. Adaire Nehring, Rellie M. Goddard

Writing—review & editing: Diède Hein, Kathryn M. Kumamoto, Haiyan Chen, M. Adaire Nehring, Rellie M. Goddard

Figure creation: Diède Hein, Kathryn M. Kumamoto, Haiyan Chen, M. Adaire Nehring, Rellie M. Goddard

Table creation: Diède Hein, Kathryn M. Kumamoto, Haiyan Chen, M. Adaire Nehring, Rellie M. Goddard

Software: Diède Hein, Kathryn M. Kumamoto, Haiyan Chen, M. Adaire Nehring, Rellie M. Goddard











Other contributions: Diède Hein, Kathryn M. Kumamoto, Haiyan Chen, M. Adaire Nehring, Rellie M. Goddard

© 2025. The Author(s).

This is an open access article under the terms of the [Creative Commons Attribution License](https://creativecommons.org/licenses/by/4.0/), which permits use, distribution and reproduction in any medium, provided the original work is properly cited.

Attribution License, which permits use, distribution and reproduction in any medium, provided the original work is properly cited.

The Role of Dislocations in the Anelasticity of the Upper Mantle

Diède Hein¹ , Lars N. Hansen¹ , Kathryn M. Kumamoto² , Haiyan Chen³ , M. Adaire Nehring¹ , Rellie M. Goddard⁴ , Thomas Breithaupt⁵ , Andrew J. Cross⁶ , Christopher A. Thom⁷ , and Caroline Seyler⁸ 

¹Department of Earth and Environmental Sciences, University of Minnesota, Minneapolis, MN, USA, ²Lawrence Livermore National Laboratory, Livermore, CA, USA, ³Department of Geosciences, Stony Brook University, Stony Brook, NY, USA, ⁴Department of Geology, Lakehead University, Thunder Bay, ON, Canada, ⁵Department of Earth Sciences, University of Cambridge, Cambridge, UK, ⁶Department of Geology and Geophysics, Woods Hole Oceanographic Institution, Woods Hole, MA, USA, ⁷Rhenium Alloys Inc., North Ridgeville, OH, USA, ⁸Department of Earth Sciences, University of Southern California, Los Angeles, CA, USA

Abstract Dislocation-based dissipation mechanisms potentially control the viscoelastic response of Earth's upper mantle across a variety of geodynamic contexts, including glacial isostatic adjustment, postseismic creep, and seismic-wave attenuation. However, there is no consensus on which dislocation-based, microphysical process controls the viscoelastic behavior of the upper mantle. Although both intergranular (plastic anisotropy) and intragranular (backstress) mechanisms have been proposed, there is currently insufficient laboratory data to discriminate between those mechanisms. Here, we present the results of forced-oscillation experiments in a deformation-DIA apparatus at confining pressures of 3–7 GPa and temperatures of 298–1370 K. Our experiments tested the viscoelastic response of polycrystalline olivine—the main constituent of the upper mantle—at stress amplitudes from 70 to 2,800 MPa. Mechanical data are complemented by microstructural analyses of grain size, crystallographic preferred orientation, and dislocation density. We observe amplitude- and frequency-dependent attenuation and modulus relaxation and find that numerical solutions of the backstress model match our results well. Therefore, we argue that interactions among dislocations, rather than intergranular processes (e.g., plastic anisotropy or grain boundary sliding), control the viscoelastic behavior of polycrystalline olivine in our experiments. In addition, we present a linearized version of the constitutive equations of the backstress model and extrapolate it to conditions typical of seismic-wave propagation in the upper mantle. Our extrapolation demonstrates that the backstress model can explain the magnitude of seismic-wave attenuation in the upper mantle, although some modification is required to explain the weak frequency dependence of attenuation observed in nature and in previous experimental work.

Plain Language Summary Earth's upper mantle can flow in response to forces from growing or retreating glaciers, the release of stress in the crust during earthquakes, and the waves that propagate away from earthquakes. The uplift of the land surface after major loss of ice from glaciers, the rate at which stress builds up on earthquake-generating faults, and the speed at which waves propagate away from earthquakes all depend on the rate at which the underlying mantle rocks can flow. However, those rates can change over time, and this time-dependent deformation is not well characterized for mantle rocks. To accurately predict these large-scale phenomena, we need to understand the small-scale mechanisms that control the time-dependent deformation of mantle rocks. Recent studies have proposed two models that involve microscopic crystalline defects known as dislocations. We identified the best of these models by performing laboratory experiments on synthetic mantle rocks at high pressure and temperature. We find that the behavior of these mantle rocks is most consistent with a model that involves the interactions among dislocations within the crystals that make up the rock. We further demonstrate that this model can explain important aspects of how waves generated by earthquakes travel through the mantle.

1. Introduction

The viscoelasticity of Earth's upper mantle is a key component of many geophysical processes, including mantle convection (Doin et al., 1997; Zhong et al., 2000), glacial isostatic adjustment (GIA) (Caron et al., 2017; Lau et al., 2016; Nield et al., 2018), postseismic creep (Boulze et al., 2022; Freed et al., 2012; Weiss et al., 2019), and

Software: Diede Hein, Kathryn M. Kumamoto

Supervision: Lars N. Hansen

Validation: Diede Hein

Visualization: Diede Hein

Writing – original draft: Diede Hein

Writing – review & editing: Lars

N. Hansen, Kathryn M. Kumamoto,

M. Adaire Nehring, Rellie M. Goddard,

Thomas Breithaupt, Andrew J. Cross,

Christopher A. Thom, Caroline Seyler

seismic-wave attenuation (Cammarano & Romanowicz, 2008; Priestley & McKenzie, 2013). Confident prediction and analysis of these processes requires a rheological model based on a sound understanding of the microphysical mechanisms involved in the deformation of the upper mantle. However, rheological models for the mantle are often limited in that they either only consider steady-state behavior or are empirical in nature.

It is common practice to simplify the rheological behavior of the upper mantle to a Maxwell model, which assumes an instantaneous elastic response and a long-term, steady-state viscosity (e.g., Klein et al., 2016; Yuen et al., 1986). Such a simplification may be reasonable for processes that occur over long timescales like mantle convection (Lau & Holtzman, 2019). However, a Maxwell model cannot explain the time-dependent evolution of the apparent viscosity of the upper mantle, often referred to as “transient” rheological behavior, that has been inferred by recent studies of postseismic creep (Freed et al., 2012; Muto et al., 2019; Weiss et al., 2019). It has also been argued that discrepancies in upper-mantle viscosity estimates among GIA studies may result from the simplification of the rheological behavior of the mantle to a Maxwell model (Caron et al., 2017; Lau & Holtzman, 2019).

Alternatively, a Burgers model (i.e., an anelastic, Kelvin-Voigt element in series with a Maxwell model) can produce an apparent change in viscosity over time and therefore may better describe observations of postseismic creep and GIA. However, a variety of conflicting types of Burgers models have been proposed, including linear (Pollitz, 2003, 2005) and nonlinear (Freed et al., 2012; Masuti & Barbot, 2021) versions. Furthermore, many Burgers models are empirical in nature, lacking any explicit link to the microphysics of deformation. Without a microphysical basis, these empirical models are not generalizable to the wide range of timescales and strain amplitudes associated with the variety of Earth processes. Simply put, a Burgers model calibrated for postseismic creep in one location may not be applicable to seismic-wave attenuation in that same location, nor can it be applied to postseismic creep in other localities with different thermomechanical conditions. This limitation highlights the need for a general physical understanding of the mechanisms that control viscoelasticity of the upper mantle across a wide range of timescales and strain amplitudes.

Unfortunately, the experimental community has not yet reached consensus on which microphysical mechanism controls the viscoelasticity of polycrystalline olivine, the predominant phase in Earth's upper mantle. Geophysical observations indicate that attenuation, denoted by Q^{-1} , in the upper mantle is on the order of 10^{-3} – 10^{-2} and depends weakly on frequency, with $Q^{-1} \propto \omega^{-\alpha}$, in which ω is frequency and $\alpha \lesssim \frac{1}{3}$ (Anderson & Minster, 1979; Gribb & Cooper, 1998; Lekić et al., 2009; Ma et al., 2020). To date, however, most experimental work has focused solely on attenuation at seismic-wave frequencies and amplitudes. Under such conditions, early forced torsional oscillation experiments on fine-grained polycrystalline olivine produced a similar, weak frequency dependence, an inverse dependence of attenuation on grain size, and linear viscoelastic behavior (Faul & Jackson, 2015; Gribb & Cooper, 1998; Jackson & Faul, 2010), consistent with elastically, diffusionally-assisted, and diffusionally-accommodated grain-boundary sliding attenuation mechanisms (Morris & Jackson, 2009). The observed behavior can be described with an extended Burgers model (i.e., a Burgers model with multiple Kelvin-Voigt elements in series; Jackson & Faul, 2010). However, recent forced torsional oscillation experiments covering a wider range of grain sizes by Qu (2022) revealed a significantly greater grain-size sensitivity of attenuation than previously reported. Therefore, extrapolation of the extended Burgers model to upper-mantle conditions is problematic as it underpredicts the magnitude of attenuation observed in seismic-wave studies by at least an order of magnitude. As such, grain-boundary sliding mechanisms alone may not be able to account for the observed seismic-wave attenuation in the upper mantle (Qu, 2022). We note that experiments on analog materials indicate that dissipation by grain-boundary sliding may be enhanced by the presence of impurities on grain boundaries (Takei, 2022) or the pre-melting effect at high homologous temperature (Yamauchi & Takei, 2016, 2024), but these effects have yet to be quantified for olivine. Hence, despite the significant amount of progress made on the problem of seismic-wave attenuation in polycrystalline olivine, it appears that additional microphysical mechanisms may need to be considered to explain the viscoelastic behavior of the upper mantle.

As an alternative to mechanisms involving sliding along grain boundaries, dislocation-based mechanisms may be able to simultaneously explain the observed magnitudes of seismic attenuation, as well as the inferred changes in the apparent viscosity of the upper mantle during postseismic creep and GIA. The large stress changes associated with these processes in particular (up to several MPa) likely activate the motion and multiplication of dislocations, and the role that dislocations play in the attenuation of seismic waves in the upper mantle is the subject of ongoing research (Farla et al., 2012; Gueguen et al., 1989; Sasaki et al., 2019; Tero & Nakajima, 2024, 2025). Two recent

dislocation-based microphysical models have been proposed to explain the viscoelastic response of the upper mantle, one based on stress heterogeneity and interactions among grains (Karato, 2021), hereafter referred to as the “plastic-anisotropy model,” and one based on long-range interactions among dislocations, termed backstress, within grains (Breithaupt et al., 2023; Hansen et al., 2021), hereafter referred to as the “backstress model.” While other microphysical models involving dislocations have been proposed that link changes in grain size to the transient rheological behavior of the upper mantle (Holtzman et al., 2018; Mulyukova & Bercovici, 2022), these models cannot produce the anelastic behavior that is required to explain seismic-wave attenuation and is potentially important for postseismic creep and GIA. Therefore, we focus our analyses on the plastic-anisotropy and backstress models.

Thus far, the plastic-anisotropy and backstress models have been tested and calibrated in the time domain (Ashby & Duval, 1985; Breithaupt et al., 2023; Hansen et al., 2019, 2021; Karato, 2021), in which a constant stress (strain rate) is applied, and an evolving strain rate (stress) is measured. However, the subtle differences in the short-term viscoelastic response among viscoelastic models are challenging to resolve in experiments in the time domain. These difficulties are compounded in high-pressure experiments, where a tradeoff exists between the time resolution and the precision of stress measurements. These differences can be more easily probed in the frequency domain, in which an oscillatory stress may be applied at a particular frequency for many cycles (Cooper, 2002; Faul & Jackson, 2015). Therefore, dynamic (i.e., “oscillatory”) testing of the response of polycrystalline olivine at stress amplitudes high enough to activate dislocation-based mechanisms is necessary for distinguishing which of the available models is most applicable to the upper mantle.

Here we present high-stress, forced-oscillation experiments at high pressure and various temperatures that characterize, for the first time, the nonlinear viscoelastic behavior of polycrystalline olivine. We conducted experiments using a deformation-DIA (D-DIA) apparatus coupled with synchrotron X-ray radiography and diffraction. The D-DIA is capable of performing forced-oscillation tests up to gigapascal stress amplitudes (Li & Weidner, 2007, 2010), thereby permitting investigation of the physics of the proposed dislocation-based mechanisms that dissipate energy during cyclic deformation. Combined with detailed microstructural analysis, the experiments were designed to test the dynamic viscoelastic response of polycrystalline olivine as a function of temperature, frequency, stress amplitude, grain size, and dislocation density. We find that our results are consistent with numerical solutions of the backstress model and argue that intragranular interactions among dislocations may explain the viscoelastic behavior of the upper mantle. We derive and extrapolate a linearized version of the backstress model to conditions of seismic waves propagating through the upper mantle and discuss the potential role of dislocations in seismic-wave attenuation.

2. Theoretical Background

2.1. Viscoelastic Behavior in the Frequency Domain

During dynamic testing, the dissipation of strain energy produces attenuation, Q^{-1} , and changes in effective modulus, E_{eff} , as a function of frequency, ω , and sometimes stress amplitude, σ_A . Attenuation is defined as the tangent of the loss angle, δ , which is the phase lag between the stress and strain during dynamic testing,

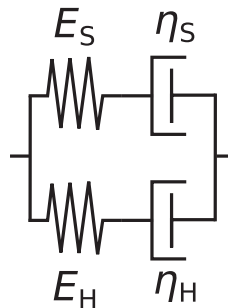
$$Q^{-1} = \tan(\delta), \quad (1)$$

or as the ratio of energy dissipated to energy stored per quarter cycle,

$$Q^{-1} = \frac{1}{2\pi} \frac{\Delta E}{E_{\text{stored}}}, \quad (2)$$

in which ΔE is the energy dissipated and E_{stored} is the energy stored. Note that the attenuation values reported in this work are associated with uniaxial shortening deformation, sometimes denoted by Q_E^{-1} , where the subscript E refers to the Young's modulus. This quantity is not necessarily equal to the attenuation associated with shear deformation, Q_μ^{-1} , which is the quantity typically of interest in seismic shear-wave attenuation. However, in our nominally melt-free samples the contribution of bulk attenuation (i.e., the attenuation associated with volumetric

Plastic-anisotropy model



Backstress model

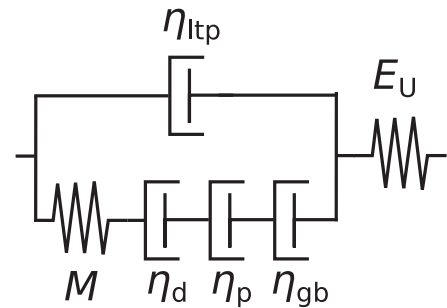


Figure 1. Spring and dashpot representations of the plastic-anisotropy model (left) and the backstress model (right). In the plastic-anisotropy model, subscripts S and H refer to the soft and hard slip systems, respectively, and E_S and E_H denote the unrelaxed directional Young's modulus and the steady-state viscosity of the slip system, respectively. For the backstress model, η_{ltp} is the viscosity associated with low-temperature plasticity, M is the hardening modulus, η_d , η_p , and η_{gb} represent dynamic recovery, recovery by pipe diffusion, and recovery by grain-boundary diffusion, respectively, and E_U is the unrelaxed Young's modulus. Note that all of the dashpots have non-Newtonian viscosities.

deformation) to Q_E^{-1} is minimal, so Q_E^{-1} provides a decent approximation of shear attenuation (McCarthy et al., 2011).

The simplest viscoelastic model, that of the linear Maxwell solid, produces attenuation that is inversely proportional to frequency, $Q^{-1} \propto \omega^{-1}$. Such behavior is hereafter referred to as Maxwell-type background dissipation. More complicated viscoelastic models include one or more anelastic elements that produce a Debye peak, i. e., a local maximum in attenuation magnitude as a function of frequency, the location of which is defined by its characteristic Maxwell frequency. The height of the Debye peak is proportional to the relaxation strength of the anelastic element. Multiple closely spaced Debye peaks can lead to a weak dependence of attenuation on frequency. For reference, Figure 1 in Karato and Spetzler (1990) provides a schematic illustration of $Q^{-1}(\omega)$ and $E_{eff}(\omega)$ of a linear Maxwell solid and a standard linear solid as examples of viscous and anelastic behaviors, respectively. For further background on the relation between time- and frequency-dependent viscoelastic behavior, the reader is referred to the texts of Lakes (2009) and Nowick and Berry (1972).

2.2. Linear Versus Nonlinear Viscoelastic Behavior

Linear viscoelastic models are composed of linear viscous and linear elastic components. For these models, analytical solutions for Q^{-1} as a function of frequency are available (e.g., Qausar, 1989). Linear viscoelastic models lead to attenuation that is independent of amplitude. However, deformation accommodated by dislocation-based mechanisms usually results in nonlinear viscoelasticity and therefore may lead to amplitude-dependent attenuation. The behavior of nonlinear viscoelastic rheological models is typically investigated numerically as analytical solutions for Q^{-1} are often unavailable.

2.3. Plastic-Anisotropy Model

The plastic-anisotropy model considers the time-dependent relaxation of displacement incompatibilities along grain boundaries following a change in stress orientation or deformation geometry in a plastically anisotropic medium (Ashby & Duval, 1985; Karato, 2021). During progressive deformation, and assuming a homogeneous strain distribution upon deformation, these incompatibilities are first accommodated by anisotropic elastic deformation, then by dislocation creep of grains that are favorably oriented for slip on soft slip systems, and ultimately by dislocation creep of grains that are oriented such that they require activation of hard slip systems, the latter of which control steady-state deformation. This sequence thus produces an increase in apparent viscosity with an increase in strain. As illustrated in Figure 1, this model can be visually represented by two nonlinear Maxwell models in parallel, with one Maxwell model representing the soft slip system and the other Maxwell model representing the hard slip system. Note that viscosities used for each slip system are assumed to be the

viscosities measured at steady state in experiments on single crystals (Karato, 2021) even though single crystals exhibit an evolution of the apparent viscosity prior to reaching steady state (Cooper et al., 2016; Hansen et al., 2021; Hanson & Spetzler, 1994). The overall strain rate, $\dot{\epsilon}$, can thus be expressed as

$$\dot{\epsilon} = \frac{\dot{\sigma}_S}{E_S} + A_S \sigma_S^n = \frac{\dot{\sigma}_H}{E_H} + A_H \sigma_H^n, \quad (3)$$

in which E_x is the directional Young's modulus for a crystal oriented for slip on the x th slip system, A_x is a pre-exponential factor incorporating the effects of temperature, pressure, and oxygen fugacity on dislocation creep, σ_x is the applied stress acting on the slip system, and n is a stress exponent. Subscripts S and H denote the soft and hard slip systems, respectively. Note that the area fractions of soft and hard slip systems are assumed to be equal. Equation 3 can be rewritten into a set of coupled ordinary differential equations as

$$\dot{\epsilon} = \frac{1}{(E_S + E_H)} \left(2\sigma + E_S A_S \sigma_S^n + E_H A_H (2\sigma - \sigma_S)^n \right) \quad (4)$$

and

$$\dot{\sigma}_S = E_S \left(\dot{\epsilon} - A_S \sigma_S^n \right), \quad (5)$$

in which σ is the applied stress (the average of σ_S and σ_H) and $\dot{\sigma}$ is the applied stress rate.

2.4. Backstress Model

Alternatively, Breithaupt et al. (2023) developed a model of dislocation-based deformation that explains the change of apparent viscosity with increasing strain via intragranular strain-energy dissipation based on the Kocks-Mecking-Estrin model for low-temperature plasticity of metals. This model is augmented with terms for dynamic recovery, static recovery of dislocations via pipe diffusion and grain-boundary diffusion, and a flow law that describes the competition between dislocations acting as carriers of deformation and dislocations interacting to produce a backstress that counteracts dislocation motion (Hansen et al., 2019, 2021). In the backstress model, the plastic strain rate, $\dot{\epsilon}_p$, is expressed as a function of dislocation density and backstress such that

$$\dot{\epsilon}_p = A(T) \rho \sinh \left(\frac{\sigma - \sigma_b}{\sigma_{\text{ref}}(T)} \right), \quad (6)$$

in which $A(T)$ is a pre-exponential factor with an Arrhenius-type temperature dependence incorporating the activation energy of dislocation glide, ρ is dislocation density, σ is the applied stress, σ_b is the backstress, and $\sigma_{\text{ref}}(T)$ is a temperature-dependent reference stress. The strain rate is approximately linearly or exponentially dependent on the effective stress, $\sigma_{\text{eff}} = \sigma - \sigma_b$, if σ_{eff} is smaller than or much larger than this reference stress, respectively. This reference stress relates to the height of the Peierls barrier, Σ , temperature, T , and the activation energy for glide, ΔF , as

$$\sigma_{\text{ref}}(T) = \frac{\Sigma RT}{\Delta F}. \quad (7)$$

Meanwhile, the backstress term in Equation 6 is composed of two terms,

$$\sigma_b = \sigma_\rho + \sigma_d, \quad (8)$$

in which the Taylor stress, σ_ρ , arises from long-range elastic dislocation interactions and relates to dislocation density through the Taylor equation,

$$\sigma_\rho = \alpha \mu b \sqrt{\rho}, \quad (9)$$

in which α is the Taylor constant, μ is the shear modulus, and b is the Burgers vector. In Equation 8, σ_d represents the grain-size sensitive threshold stress for operating a Frank-Read source that relates to grain size, d , as

$$\sigma_d = \beta \mu b / d, \quad (10)$$

in which β is a geometrical constant on the order of unity.

As the dislocation density in Equation 6 can be related to the Taylor stress through the Taylor equation, the plastic strain rate can be expressed in terms of backstress, giving

$$\dot{\epsilon}_p = A'(T) \sigma_\rho^2 \sinh \left(\frac{\sigma - \sigma_\rho - \sigma_d}{\sigma_{\text{ref}}(T)} \right), \quad (11)$$

in which $A'(T)$ is a pre-exponential factor with an Arrhenius-type temperature dependence with absorbed constants from the Taylor equation following Equation 26 of the supplementary information of Breithaupt et al. (2023).

Assuming that the contribution of lattice diffusion to static recovery is negligible, the Taylor-stress rate, $\dot{\sigma}_\rho$, can be expressed following Equation 25 of the supplementary information of Breithaupt et al. (2023) as

$$\dot{\sigma}_\rho = M \left(\frac{\sigma_\rho + \sigma_d}{\sigma_\rho} \dot{\epsilon}_p - \frac{\sigma_\rho}{\sigma_{\rho, \text{max}}} |\dot{\epsilon}_p| - R_p(T) \sigma_\rho^5 - R_{\text{gb}}(T) \sigma_\rho^3 \sigma_d \right), \quad (12)$$

in which M is the hardening modulus, $\sigma_{\rho, \text{max}}$ is the maximum Taylor stress, and R_p' and R_{gb}' are pre-exponential factors each with an Arrhenius-type temperature dependence incorporating the activation energy of pipe and grain-boundary diffusion, respectively. Note that the first term on the RHS of Equation 12 represents the generation of backstress resulting from strain-driven dislocation multiplication and long-range dislocation interactions, the second term represents dynamic recovery, and the third and fourth terms represent the removal of backstress by recovery through grain-boundary diffusion and pipe diffusion, respectively.

Figure 1 provides a visual representation of Equations 11 and 12, with a parallel combination of a dashpot for low temperature plasticity as described by Equation 11, and a spring with three dashpots in series with one dashpot for each of the three recovery mechanisms. The spring represents the elastic backstress arising from long-range dislocation interactions that counteract the applied stress. Lattice elasticity in series with the backstress model is represented by an additional spring for the unrelaxed modulus, E_U .

3. Methods

For brevity, only key methodological steps are discussed in the sections below. Please refer to Text S1 in Supporting Information S1 for more detail.

3.1. Deformation-DIA Experiments

3.1.1. Sample Synthesis

Powders of natural San Carlos olivine, containing ~1% of orthopyroxene to buffer silica activity, were dried overnight at 1000°C in a gas-mixing furnace under controlled oxygen fugacity at the Ni-NiO buffer. Dried powders were cold-pressed into Ni capsules and subjected to evacuated hot-pressing at 1250°C and a confining pressure of 300 MPa in a gas-medium apparatus (Paterson, 1990). Evacuated hot-pressing produced dense, fine-grained, nominally dry and melt-free polycrystalline olivine cylinders. Starting material was generated with two different grain size fractions. One starting material, PT1616, was synthesized following this approach, while the other starting material, PT1242, was further annealed for 68 hr at 1200°C in a gas-mixing furnace under controlled oxygen fugacity to produce coarser grains. However, as discussed below, microstructural analysis indicates that there is little difference in grain size between PT1616 and PT1242 after an initial loading and relaxation procedure (Section 4.2). Right-cylindrical cores with a diameter of 1.05–1.20 mm were extracted

parallel to the long axis of the hot-pressed cylinders using a diamond coring drill, ground to a height of 0.50 ± 0.02 mm, and squared on diamond lapping film with a grit size of 30 μm .

3.1.2. Sample Assembly

Cubic sample assemblies were constructed following the procedure outlined in (Goddard et al., 2023, their Figure 1). Each experimental column contained a vertical stack of olivine samples from starting materials PT1616 (top) and PT1242 (bottom) with the aim of providing a direct comparison of the effect of grain size on the viscoelastic response of olivine. Care was taken to match the diameters of the samples to ensure that both samples experienced the same stress (see Section 3.1.3). Samples were surrounded by Ni foils to both buffer the oxygen fugacity at the Ni-NiO buffer and to serve as strain markers for radiography during the experiments.

We used the furnace calibration of Cross et al. (2025), which relates sample temperature to the electrical power applied to the graphite resistive-heating furnace, and that was calibrated for the same nominal cell dimensions and materials as used here. We favor this calibration over using a thermocouple as the inclusion of a thermocouple in the experimental assembly can decrease its mechanical stability and introduces a heat sink that enhances thermal gradients in the assembly (Raterron et al., 2013). In addition, the inclusion of a thermocouple in the assembly does not necessarily increase temperature accuracy as displacement of the thermocouple during deformation, combined with the large thermal gradients in a D-DIA assembly, can compromise the temperature measurements (Dixon & Durham, 2018). Cross et al. (2025) found the kinetics of the quartz-to-coesite phase transformation in the D-DIA to be consistent with the calibrated temperatures, furthering our confidence in this approach. We conservatively estimate that our reported temperatures are accurate to within 50 K (see Section 5.1 for details).

3.1.3. Deformation Experiments

Synchrotron-based deformation experiments were conducted in a Deformation-DIA (D-DIA) apparatus housed at beamline 6-BM-B of the Advanced Photon Source (Argonne National Laboratory, Chicago, IL). Details of the technique are outlined elsewhere (e.g., Li & Weidner, 2010; Wang et al., 2003), and we only summarize the key details here. The D-DIA apparatus consists of six hydraulic anvils—four horizontal anvils and two vertical anvils—that can be simultaneously advanced to isostatically load the cubic sample assembly. In addition, the vertical anvils, hereafter referred to as the differential rams, can be independently advanced or retracted using hydraulic syringe pumps, enabling axial differential loading of the assembly.

White synchrotron X-rays were used to obtain stresses and strains via energy-dispersive X-ray diffraction and radiography, respectively. Energy-dispersive X-ray spectra were collected using nine solid-state detectors configured in a semi-circle around and oriented at a fixed angle to the incident X-ray beam. The energies of peaks from the 112, 131, and 130 lattice planes of olivine were converted to lattice spacing using Bragg's law. We use these diffraction peaks because they are consistently resolved even over the short diffraction collecting time during our highest-frequency forced oscillations. Differential stresses and mean stresses were then calculated from these lattice spacings and the azimuths of the detectors around the horizontal incident beam, following the approach of Weidner et al. (2010). Following Hansen et al. (2019), digital-image cross correlation of the Ni-foils in the radiographs was used to calculate axial strain of the samples. Strain resolution of this method in our experiments was on the order of 10^{-4} . Stresses and strains were computed in near-real time during the deformation experiments.

We measured stresses in the finer grained material, PT1616, assuming that both samples experienced the same stress state, allowing for faster collection of diffraction patterns and increased time resolution (Hansen et al., 2019). The MgO pressure medium surrounding the sample stack has a sufficiently low viscosity ($\sim 10^{11}$ Pas) at high pressure and temperature (Mei et al., 2008) such that any strength differences between olivine samples do not significantly compromise the assumption that the stress state is homogeneous (Silber et al., 2022). This assertion is further supported by a clear deviation from iso-strain conditions in the experiments (i.e., strain rates vary significantly between the samples during deformation).

At the start of each experiment, the assembly was pressurized by loading the D-DIA with the main ram up to a load of 30–50 tons over the course of an hour, which resulted in a confining pressure of 3–7 GPa. After pressurization, electrical power through the assembly was increased to reach the target temperature. Then, the differential rams were advanced to compress the samples to shortening strains of 0.1–0.2 at a syringe pump rate of

0.01 mm s^{−1}, corresponding to a strain rate of $\sim 10^{-4}$ s^{−1}. The syringe pumps were then stopped, and stress was allowed to relax for 10–20 min. The stress relaxed to approximately zero for experiments with a target temperature >1000°C. Stress relaxation was incomplete in our experiments at 900°C and negligible in our experiments at room temperature. After relaxation, the assembly was subjected to axial forced oscillations using the “*Sinepump*” software available at beamline 6-BM-B, which imposed sinusoidal actuation of the syringe pumps at frequencies of 10^{−4} to 10^{−2} Hz (Li & Weidner, 2007).

Details of all experiments are summarized in Table 1. In the experiments presented here, we stepped through either stress amplitude or frequency to test the dependence of attenuation and effective modulus on those variables. Steps in stress amplitude were performed by varying the stroke length of the syringe pumps. In frequency-stepping experiments, the amplitude of the syringe pump was adjusted for each step with the aim of keeping the stress amplitude constant. Each step typically consisted of a set of approximately 10 or more oscillations. Note that, due to the hydraulic actuation of the D-DIA, stress or strain amplitude could only be controlled indirectly. In addition, we could not control the average stress experienced by the samples during a forced oscillation, hereafter referred to as the bias stress, σ_{dc} . This bias stress relaxed over the course of several oscillations in high-temperature experiments. Hence, care was taken to achieve stable oscillatory behavior at each step before continuing to the next step. At the end of each experiment, the sample was quenched by cutting power to the furnace, followed by depressurization over the course of at least an hour.

For one experiment, SAN 626, the sample assembly was subjected to pressurization, heating, initial compression, and stress relaxation, after which the sample was quenched and depressurized without any additional deformation. This experiment served as a reference for the microstructural state of our samples at the start of forced oscillations in the other experiments.

3.2. Mechanical and Microstructural Analyses

3.2.1. Mechanical Analysis

To analyze the mechanical data, we subdivided each timeseries into intervals of stable oscillatory behavior for each amplitude or frequency step. We then fit these subsets with sinusoids superposed on polynomial trends, detrended the fits, and extracted a value of attenuation and effective modulus for each subset. We calculated Q^{-1} from the phase lag between the best-fit sinusoids for the detrended stress and strain data following Equation 1. Due to the limited time resolution of our measurements, we did not resolve any harmonic distortion of the strain signal. Therefore, this fitting approach with simple sinusoids suffices to quantify attenuation from these data. The effective Young's modulus was calculated from the detrended best-fit sinusoids for stress and strain as

$$E_{\text{eff}} = \frac{\sigma_{\text{max}}}{\epsilon_{\text{max}}}. \quad (13)$$

Figure 2 provides an illustrative example of this procedure.

Errors on Q^{-1} and E_{eff} are associated with the quality of the fit to the stress and strain data. To account for the complex coupling among the uncertainties of the polynomial trend and those of phase and amplitude, we estimated our errors using a Monte-Carlo error analysis for each set of oscillations. For each parameter of the best-fit sinusoid, we generated a random normal distribution with the two-sigma level of confidence defined by the parameter's 95% confidence interval. We then created 500 simulated timeseries of stress and strain using parameters randomly picked from these distributions and calculated Q^{-1} and E_{eff} for each simulated timeseries. These simulations yielded distributions of Q^{-1} and E_{eff} . The reported errors on Q^{-1} and E_{eff} are the standard deviation of these distributions, which reflects the quality of the fit to the data. Please refer to Text S1.3 in Supporting Information S1 for more details of the fitting and error-analysis procedures.

3.2.2. Electron Backscatter Diffraction

We investigated the microstructures of the starting materials and deformed samples using electron backscatter diffraction (EBSD). We polished transverse sections of the hot-pressed samples that constituted the starting materials and longitudinal axial sections of the deformed samples using progressively finer diamond lapping films down to 0.5 μm grit size followed by a 3–10 min Syton finish. EBSD analysis was performed under low-vacuum

Table 1
Summary of Key Experimental Parameters

Exp.	Procedure	T_t , target temperature (°C)	Time at elevated temperature (hr)	Main press load (ton)	Confining pressure ^a (GPa)	ω , frequency ^b (Hz)	<i>Sinepump</i> amplitude ^b (mm)	σ_A , stress amplitude ^{a,b} (MPa)	σ_{dc} , bias stress ^{a,b} (MPa)
SAN 626	Microstructure control	1,100	0.9	50	4.6 ± 0.3	—	—	—	—
SAN 591 ^c	Frequency stepping	1,060	9.0	50	5.0 ± 0.4	1/300	3	160 ± 20	30 ± 10
						1/600	3	160 ± 10	30 ± 30
						1/1,000	3	90 ± 10	20 ± 30
						1/300	3	170 ± 30	50 ± 30
SAN 637	Frequency stepping	1,110	16.8	30	3.2 ± 0.3	1/300	3	200 ± 20	30 ± 20
						1/3,600	6	110 ± 10	10 ± 20
						1/300	3	140 ± 20	10 ± 50
						1/1,000	4.5	150 ± 30	0 ± 30
SAN 597 ^d	Amplitude stepping	1,060	1.8	50	5.4 ± 0.5	1/300	3	200 ± 50	0 ± 50
						1/1,000	5	180 ± 30	10 ± 20
						1/1,000	3	70 ± 10	20 ± 30
						1/1,000	7	260 ± 70	50 ± 70
SAN 625	Amplitude stepping	1,150	8.2	50	4.5 ± 0.4	1/1,000	5	170 ± 20	20 ± 80
						1/300	2	170 ± 10	60 ± 20
						1/300	3	230 ± 10	20 ± 10
						1/300	5	270 ± 10	10 ± 20
						1/300	3	130 ± 10	10 ± 30
						1/300	2	80 ± 10	-20 ± 10
						1/300	8	370 ± 10	10 ± 50
						1/300	2	80 ± 10	-10 ± 10
SAN 628	Amplitude stepping	900	6.8	40	4.9 ± 0.8	1/300	2	480 ± 10	840 ± 160
						1/300	4	790 ± 70	260 ± 90
						1/300	6	880 ± 30	40 ± 110
						1/300	2	280 ± 20	-20 ± 30
						1/300	8	$1,230 \pm 90$	30 ± 20
						1/300	2	360 ± 10	-250 ± 40
SAN 630	Amplitude stepping	25	0	30	6.7 ± 0.8	1/300	4	$1,660 \pm 70$	2740 ± 80
						1/300	2	790 ± 30	-300 ± 320
						1/300	4	$1,760 \pm 70$	130 ± 290
						1/300	6	$2,810 \pm 150$	940 ± 180
						1/300	2	910 ± 10	$2,580 \pm 40$

^aStress values presented here are the average of the stress estimates of the three lattice planes. Error estimates are the standard deviation of these stress estimates and reflect the variability of stress estimates among the three lattice planes. ^bEntries are listed in chronological order. ^cSynchrotron beam was lost for an interval of 1 hr during the first frequency step. Mechanical data from before and after this interval are reported separately in Figure 3. ^dA sudden decrease in stress and strain amplitude occurred halfway through the third amplitude step, which did not correspond to a change in *Sinepump* settings. Mechanical data from before and after this change are reported separately in Figure 4 and Figure S1 in Supporting Information S1.

conditions in a Thermo Fisher Scientific Apreo 2S Lo-Vac scanning electron microscope (SEM) equipped with an Oxford Instruments Symmetry EBSD detector and AZtec data acquisition software at the University of Minnesota. Further acquisition details are summarized in Table S1 of Supporting Information S1. We processed the EBSD data using AZtecCrystal. In this processing, we first removed wild spikes and filled non-indexed pixels with an orientation corresponding to the average of their 8 nearest neighbors. We then corrected for systematic misindexing related to the hexagonal pseudosymmetry of olivine with $60 \pm 5^\circ$ rotations around [100]. Finally, we

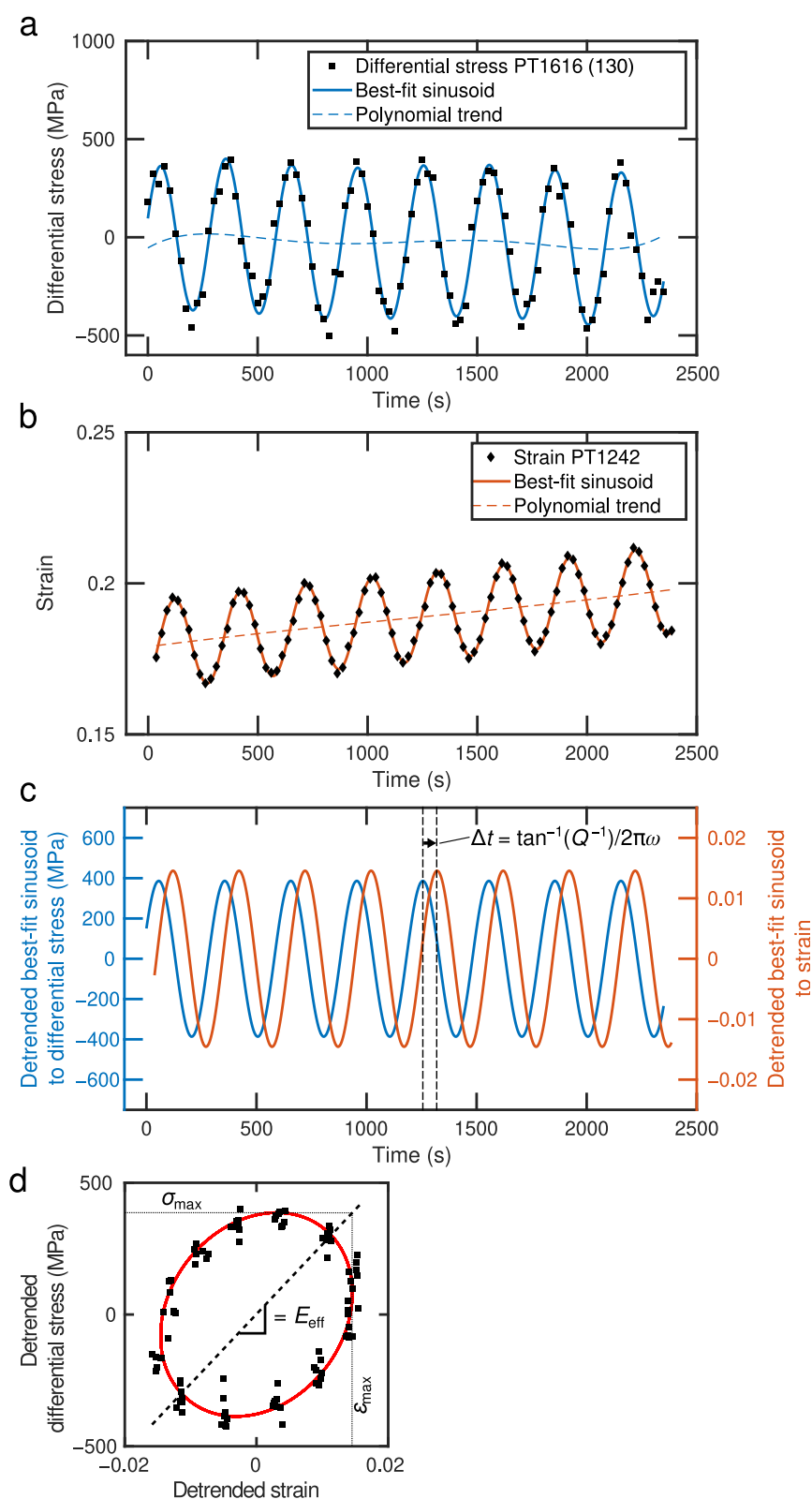


Figure 2.

performed 10 iterations of filling non-indexed pixels with orientations corresponding to the average of their 7, and then 6, nearest neighbors.

We characterized grain size from the EBSD data by means of the linear-intercept method using MTEX (Goddard et al., 2020). We used a minimum misorientation angle for grain boundaries of 15° and applied a stereographic correction factor of 1.5 to the arithmetic mean to obtain the mean grain size (Underwood, 1970, p. 81). To characterize grain-size variation within each starting material, we collected EBSD data in the center and near the edge of transverse sections of each cylindrical hot-press. Further details are outlined in Text S1.4.1 of Supporting Information S1.

Crystallographic preferred orientations (CPOs) were extracted from EBSD data using MTEX (Bachmann et al., 2010). For this analysis, we reconstructed the grains based on a minimum misorientation angle of 15° and removed spurious grains containing <10 indexed pixels. We then produced pole figures of crystallographic orientations using one point per grain. We quantify CPO strength using the M-index (M), which is equal to 1 when all grain orientations are identical, and tends to 0 for an aggregate with randomly distributed grain orientations. Note that we calculated the M-index using code written by Billings and Skemer (2024), following the original approach of Skemer et al. (2005), rather than by using the in-built MTEX functionality. Skemer et al. (2005) calculated M using the misorientation-angle distribution, whereas MTEX calculates M using the orientation distribution function. We verified that the number of grains was sufficient to provide reliable M-indices for each EBSD map following the approach of Skemer et al. (2005).

3.2.3. Dislocation Decoration and Dislocation Density Analysis

Following EBSD analysis, we decorated dislocations in the samples (Karato, 1987; Kohlstedt et al., 1976), carefully removed the oxidation rind using diamond lapping film, and coated the samples with 10 nm of carbon for SEM analysis. We acquired backscattered-electron images of decorated dislocations under high-vacuum conditions using a JEOL-SEM 8530F microprobe located at the University of Minnesota. We imaged the decorated dislocations at $6,000\times$ – $43,000\times$ magnification, typically capturing 1–5 grains per image. We imaged two or three adjacent areas in each sample to capture spatial variability. Images were taken in the center of each sample and away from areas with decompression cracks.

Images were divided into subregions with areas of $12\text{--}75\text{ }\mu\text{m}^2$ depending on their magnification. We counted the dislocations in these subregions by hand and estimated dislocation density by dividing the number of dislocations over the area of the subregion. The reported errors reflect the standard deviation among the different subregions. Please refer to Text S1.4.2 in Supporting Information S1 for more details. Decorated dislocations that appeared to be organized into tilt walls were excluded from the dislocation-density measurement. In total, approximately 41,000 dislocations were counted over an area of $5,400\text{ }\mu\text{m}^2$ divided over 13 samples.

3.3. Numerical Modeling of Constitutive Equations in the Frequency Domain

To compare the plastic-anisotropy and backstress models to data from our experiments, we evaluate Equations 4 and 5 and Equations 11 and 12, respectively. We numerically solved these stiff model equations using the Matlab® function *ode15s* for an imposed sinusoidal stress at a prescribed bias stress, σ_{dc} , frequency, ω , and stress amplitude, σ_A . For the backstress model, we calculated the elastic strain separately and added it to the plastic strain. Generated timeseries of strain were detrended using low-order polynomials and attenuation and effective modulus measurements were made from the part of the timeseries at which the background strain rate had reached steady-state. We used the maximum stress and strain of the detrended timeseries to calculate the effective modulus following Equation 13. The dissipated energy per cycle, ΔE , was calculated by trapezoidal numerical integration of the stress-strain hysteresis loops, and the stored energy, E_{stored} , was calculated as $E_{\text{stored}} = \frac{1}{2}\sigma_A^2/E_U$.

Figure 2. Illustrative example of the fitting of our mechanical data and extraction of Q^{-1} and E_{eff} for amplitude-step 6 of experiment SAN 625, sample PT1242. Panel (a) presents the timeseries of differential stress that was calculated from the lattice spacings of the PT1616 sample (only data from (130) are illustrated here for simplicity), and panel (b) presents the associated strain timeseries. Solid lines illustrate the best-fit sinusoids to the data, and dashed lines indicate the polynomial trend of this best-fit sinusoid. Panel (c) presents the detrended best-fit sinusoids to illustrate the time delay, Δt , that results from the phase lag between the differential stress and strain. The tangent of the phase lag is proportional to attenuation, Q^{-1} , following Equation 1. Panel (d) illustrates the associated hysteresis loop. The red solid line represents the hysteresis loop obtained from the detrended best-fit sinusoids. Annotations on panel (d) schematically illustrate how the effective modulus is obtained from the best-fit sinusoids.

following Gremaud (2001, Equation 3.3.23), which assumes that the elastic contribution to the maximum stored energy far outweighs its anelastic part. Attenuation was then calculated following Equation 2. Figure S4 of Supporting Information S1 provides an illustrative example of our numerical approach for one particular combination of parameters applied to the plastic-anisotropy model.

To make quantitative predictions for the plastic-anisotropy model, we take steady-state creep values for A_x and n from experiments on oriented single crystals of San Carlos olivine by Bai et al. (1991) at the orthopyroxene and Ni-NiO buffers for the [100](010) and [001](010) slip systems of olivine to represent the soft and hard slip systems, respectively. Oxygen fugacity, f_{O_2} , at the Ni-NiO buffer was calculated as a function of temperature and pressure using the equation outlined in Table 5 of Huebner and Sato (1970). Directional Young's moduli for San Carlos olivine for [110]c and [011]c orientations were calculated using MTEX (Bachmann et al., 2010) based on elastic constants at room temperature and ambient pressure from Abramson et al. (1997). In the limit of infinite frequency, we assume that the directional Young's moduli, E_S and E_H , must average to equal the unrelaxed modulus of a polycrystalline aggregate. Therefore, we set $E_S/E_H = E_{[110]c}/E_{[011]c}$, and $E_U = (E_S + E_H)/2$. The unrelaxed Young's modulus was calculated using the pressure and temperature derivatives from Abramson et al. (1997) and Isaak (1992), respectively. We note that the elastic anisotropy only has a minor effect on the behavior of the model as detailed in Text S2.1.1 and Figure S8 of Supporting Information S1. Table S2 in Supporting Information S1 lists the applied model parameters.

4. Results

4.1. Attenuation and Modulus Relaxation

Our frequency-stepping experiments reveal that attenuation and effective modulus change as a function of frequency. Experiment SAN 637 indicates that attenuation decreases with an increase in frequency, with $Q^{-1} \propto \omega^{-1}$ below a frequency of $\sim 10^{-3}$ Hz (Figure 3a). Experiments SAN 637 and SAN 591 both indicate that this frequency dependence of Q^{-1} weakens above $\sim 10^{-3}$ Hz (Figures 3a and 3c). Effective modulus increases strongly as frequency increases (Figures 3b and 3d). The stress amplitude did not vary more than half a decade among frequency steps (Figure 3e), so any effect of stress amplitude on attenuation or modulus relaxation in our frequency-stepping experiments is likely small. Reproducibility of Q^{-1} and E_{eff} for repeat steps within an experiment is within error of the measurement, with exception of frequency-step 5 of SAN 637 (Figure 3a), which produced stronger attenuation by approximately half a decade for lattice planes (130) and (131) than the two previous steps at that frequency at otherwise similar conditions.

Our amplitude-stepping experiments demonstrate correlations of Q^{-1} and modulus relaxation with increasing stress amplitude and temperature. Experiments SAN 625 ($T_l = 1150^\circ\text{C}$) and SAN 628 ($T_l = 900^\circ\text{C}$) demonstrate a clear positive correlation between Q^{-1} and stress amplitude when stepping up in stress amplitude (Figures 4a and 4e). The same correlation applies to modulus relaxation as a function of stress amplitude (Figures 4b and 4f). A similar amplitude dependence is less obvious for steps down in amplitude (Figure S1 in Supporting Information S1). The results of our lower-frequency experiment SAN 597 ($T_l = 1060^\circ\text{C}$) appear more ambiguous due to the deviation and uncertainty of attenuation measurements from the (112) lattice plane (triangles) compared to those from the (131) or (130) lattice planes (Figure 4c). Nevertheless, positive correlations between Q^{-1} and stress amplitude are apparent for the (131) and (130) lattice planes. At room temperature, we observe no significant modulus relaxation or correlation between Q^{-1} and stress amplitude (Figures 4g and 4h). Nevertheless, attenuation is still significant with values between 0.2 and 0.5.

4.2. Microstructures

Table 2 summarizes the key quantitative results of all microstructural analyses.

Our starting materials, PT1616 and PT1242, have significantly different mean grain sizes (Figure 5, first column). Nevertheless, the microstructure of the control experiment (SAN 626), which is representative of the microstructure at the start of forced oscillations, demonstrates that the initial difference in mean grain size does not persist over the course of the initial compression and relaxation. Instead, the grains in PT1242 recrystallized such that both samples had a similar mean grain size after the initial compression and relaxation (Figure 5, second column). We assume that the other high-temperature experiments underwent a similar grain-size evolution during

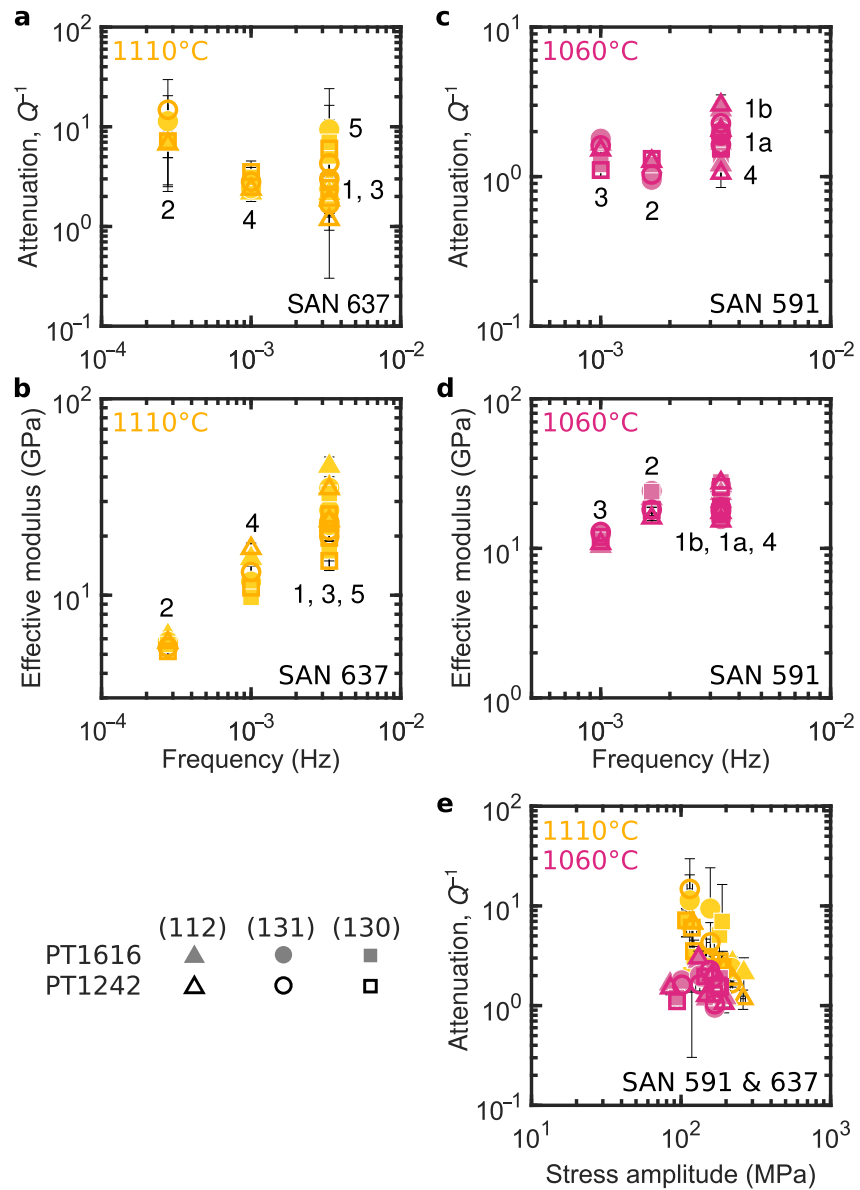


Figure 3. Results of frequency-stepping experiments SAN 637 (a, b) and SAN 591 (c, d). Annotated numbers correspond to the chronological order of the frequency steps. Suffixes b and a for step 1 of SAN 591 identify data before and after an interval of lost beam, respectively. Panel (e) presents the amplitudes corresponding to the data in panels (a–d). Error bars represent one standard deviation of the Q^{-1} and E_{eff} distributions obtained by our Monte-Carlo error analysis.

the initial compression and relaxation. In general, mean grain sizes increased moderately (less than half a decade) during forced oscillations when compared to the mean grain size of the microstructure-control experiment (see Table 2). The most extreme case of grain growth occurred during our longest high-temperature experiment, SAN 637, in which mean grain size approximately tripled (Figure 5, third column). One exception to this general trend is SAN 628, which was deformed at a relatively low temperature of 900°C and underwent a net reduction in mean grain-size (Figure 5, fourth column). Grain-size changes over the course of room-temperature experiment SAN 630 were negligible compared to the original starting microstructure (Table 2).

Our samples developed weak to modest CPO over the course of our experiments. Initially, our starting materials have weak CPO (Figure 6, first row). Microstructure-control experiment SAN 626 demonstrates that the initial compression and subsequent relaxation did not produce a strong CPO, as evidenced by M-indices of 0.02–0.03 and only minor [010] alignment with the compression direction (Figure 6, second row). After forced oscillations,

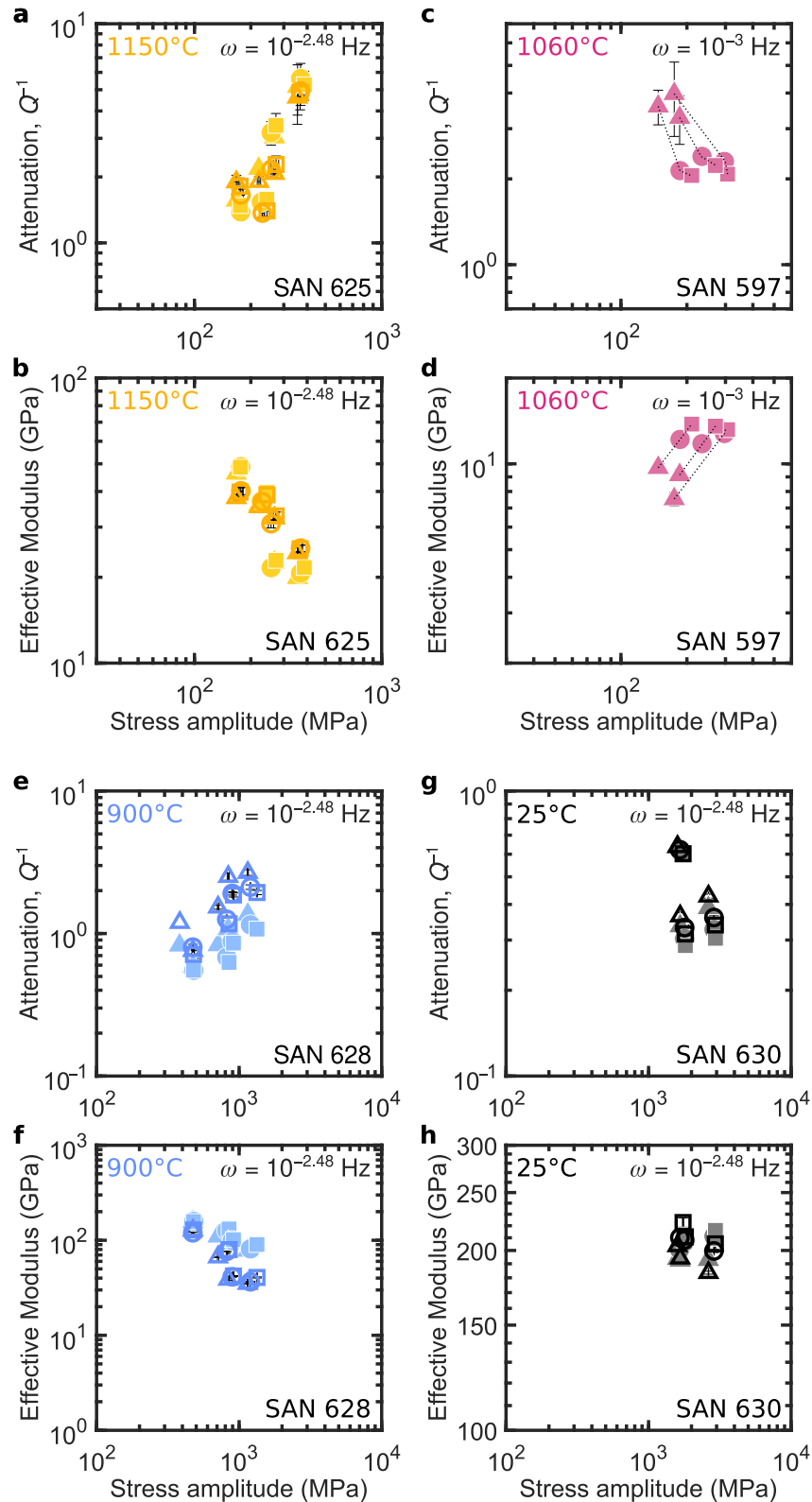


Figure 4. Results of amplitude-stepping experiments SAN 625 (a, b), SAN 597 (c, d), SAN 628 (e, f), and SAN 630 (g, h) for steps that increased in amplitude relative to the step that preceded them. The frequency of forced oscillations is indicated in the top right corner of each panel. Note that the vertical axes are scaled differently for each experiment. Dotted lines in panels (c, d) tie together data points for the three lattice planes of each amplitude step for clarity. Error bars represent one standard deviation of the distributions of Q^{-1} and E_{eff} obtained through our Monte-Carlo error analysis. Please refer to Figure 3 for explanation of symbols.

Table 2
Summary of Key Microstructural Results

Sample	Mean grain size ^a , \bar{d} (μm)	Standard deviation of intercept-length distribution (μm)	M-index	Dislocation density, ρ ($\times 10^{12} \text{ m}^{-2}$)	Final strain (%)
Starting materials					
PT1616 center	4.0	2.7	0.02	—	0
PT1616 edge	3.2	2.2	0.03	—	0
PT1242 center	20.5	10.5	0.02	—	0
PT1242 edge	15.3	9.0	0.02	—	0
Deformed samples					
SAN 591, PT1616	10.7	5.3	0.06	3.9 ± 0.8	30
SAN 591, PT1242	18.5	11.4	0.03	3.5 ± 1.0	25
SAN 597, PT1616	8.1	4.3	0.06	6.6 ± 1.9	35
SAN 625, PT1616	12.1	6.6	0.11	8.5 ± 1.3	15
SAN 625, PT1242	6.7	3.7	0.12	8.8 ± 0.8	41
SAN 626, PT1616	4.4	2.9	0.02	12.4 ± 2.9	6
SAN 626, PT1242	5.3	5.7	0.03	10.2 ± 2.8	18
SAN 628, PT1616	2.8	2.1	0.02	12.9 ± 1.4	6
SAN 628, PT1242	2.3	3.9	0.02	16.7 ± 2.0	24
SAN 630, PT1616	3.6	2.7	0.03	19.5 ± 5.8	12
SAN 630, PT1242	17.9	10.0	0.02	13.2 ± 2.4	15
SAN 637, PT1616	15.0	8.6	0.18	4.7 ± 1.6	45
SAN 637, PT1242	16.6	9.7	0.07	3.3 ± 0.8	26

^aPost-mortem mean grain sizes listed for deformed samples.

similar or stronger CPOs are observed, with M-indices ranging from 0.02 to 0.18 (see Table 2). Samples with a strong CPO feature [100] and [001] axes girdled within the compression-normal plane and [010] axes aligned with the compression axis. In general, the higher-temperature experiments (Figure 6, third and fourth row) exhibit stronger CPO than our lower-temperature experiment, SAN 628. No significant CPO developed in our room-temperature experiment, SAN 630 (Figure 6, last row).

Overall, dislocation density does not vary strongly across the full range of our experiments (Table 2). All samples exhibit dislocation densities on the order of 10^{12} – 10^{13} m^{-2} . The sample of the microstructure-control experiment, SAN 626, features relatively elevated dislocation densities on the order of $\sim 10^{13} \text{ m}^{-2}$ (Figures 7a and 7b), whereas post-experiment dislocation densities vary from 3.3×10^{12} to $20 \times 10^{12} \text{ m}^{-2}$. In general, samples from experiments with higher target temperatures (e.g., Figures 7c and 7d) exhibit lower dislocation densities than samples from experiments with lower target temperatures (e.g., Figures 7e and 7f). Long experiments at high temperature produced regular arrays of dislocations, tilt walls, and subgrain boundaries (Figure 7c).

5. Discussion

Previous micro-strain forced-oscillation studies on polycrystalline olivine typically observed behavior that was both linear and grain-size sensitive (Gribb & Cooper, 1998; Jackson & Faul, 2010) and hence disregarded dislocation-based mechanisms in favor of grain-boundary sliding mechanisms to explain their observations. Other studies reported that predeformed olivine exhibits higher attenuation than annealed olivine (Farla et al., 2012; Gueguen et al., 1989) and suggested a contribution of dislocation-based mechanisms to the viscoelastic behavior. However, they did not resolve the amplitude-dependent behavior that is diagnostic of dislocation-based dissipation mechanisms. Here, at the high stress amplitudes attainable in the D-DIA, we observe a strong increase of attenuation and modulus relaxation when increasing stress amplitude in experiments SAN 625 and SAN 628. The physical mechanisms proposed by most recent studies (i.e., elastically-

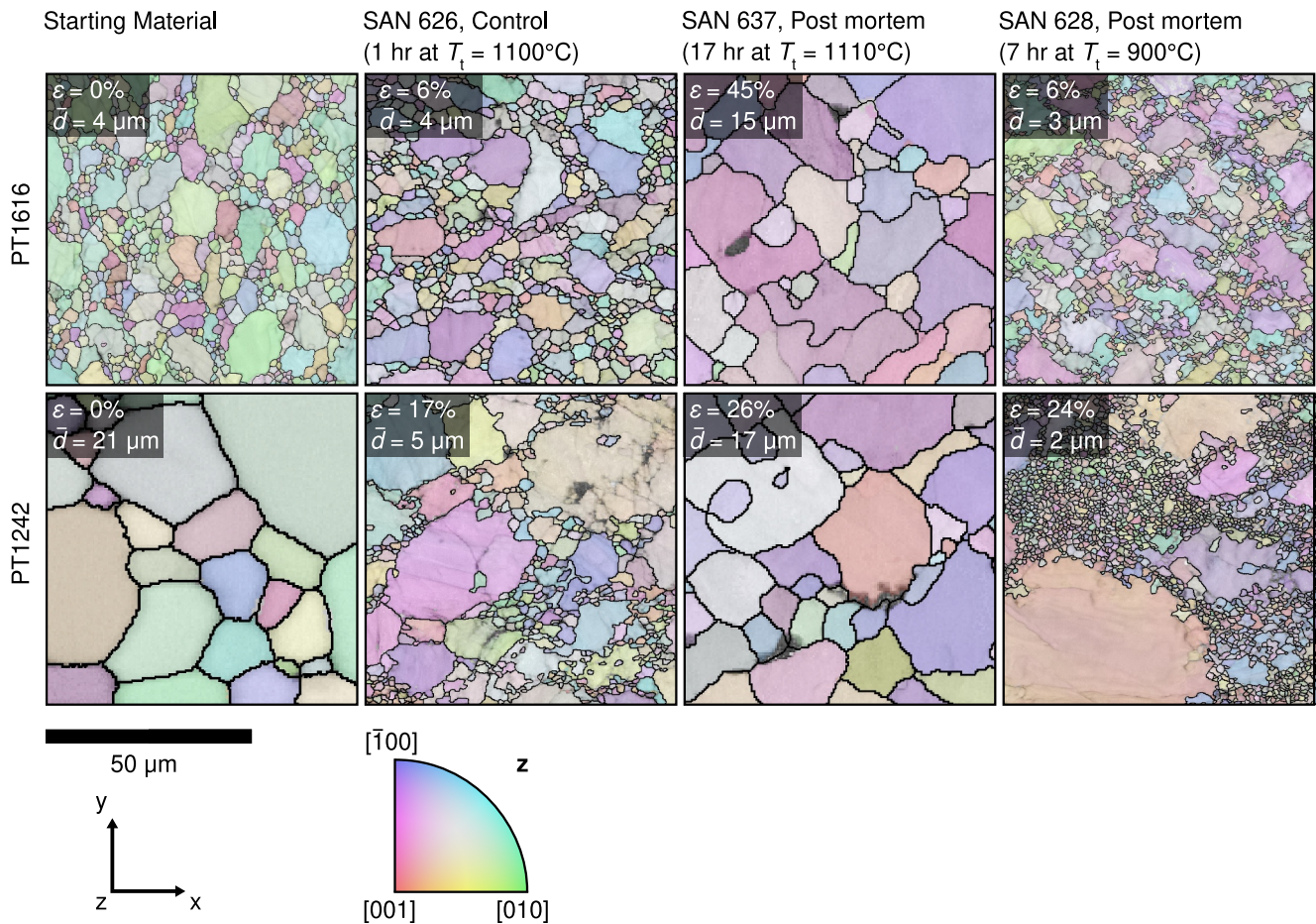


Figure 5. Band-contrast maps overlaid by crystal orientation maps and grain boundaries from representative EBSD maps. The first column illustrates the microstructures of the starting materials, the second column presents the microstructure as quenched after the initial heating, compression, and relaxation stage prior to forced oscillations, and the third and fourth columns present end-member microstructures with the coarsest and finest grain sizes after forced oscillations, respectively. Top and bottom rows are microstructures for PT1616 and PT1242, respectively. Darker regions indicate low band contrast. Crystallographic orientations are colored according to the z sample direction (i.e., perpendicular to the sample surface) relative to the inverse pole figure. The vertical direction is parallel to the compression direction for all maps other than those of the starting materials.

accommodated, diffusionally-assisted, and diffusionally-accommodated grain-boundary sliding) cannot produce such nonlinear behavior, suggesting a significant contribution of nonlinear, dislocation-based mechanisms to the viscoelastic response of the dry, nominally melt-free, polycrystalline olivine in our experiments. These results thus provide an opportunity to test existing models for dislocation-based dissipation in olivine, thereby improving our understanding of geologic processes that involve transient rheological behavior.

Here we first discuss the caveats and uncertainties of our experiments and then present a series of numerical tests to compare our data to existing models. We then present a linearized version of the most applicable model and focus on its application to existing observations of seismic attenuation in the upper mantle.

5.1. Evaluation of Experimental Conditions and the Effects of Microstructural Evolution on Viscoelastic Behavior

Temperature is the most poorly constrained variable in D-DIA experimental studies (for detailed discussions see Dixon & Durham, 2018; Raterron et al., 2013). Here we rely on the power-temperature calibration presented by Cross et al. (2025) featuring identical sample assembly materials to those employed in this study. Cross et al. demonstrated that furnace efficiency is a function of the maximum load applied to the main ram. They interpret this observation as compaction of the furnace in response to increasing confining pressure. In our experiments, confining pressure peaks at the end of the pressurization stage and is constant within ± 0.5 GPa after the initial

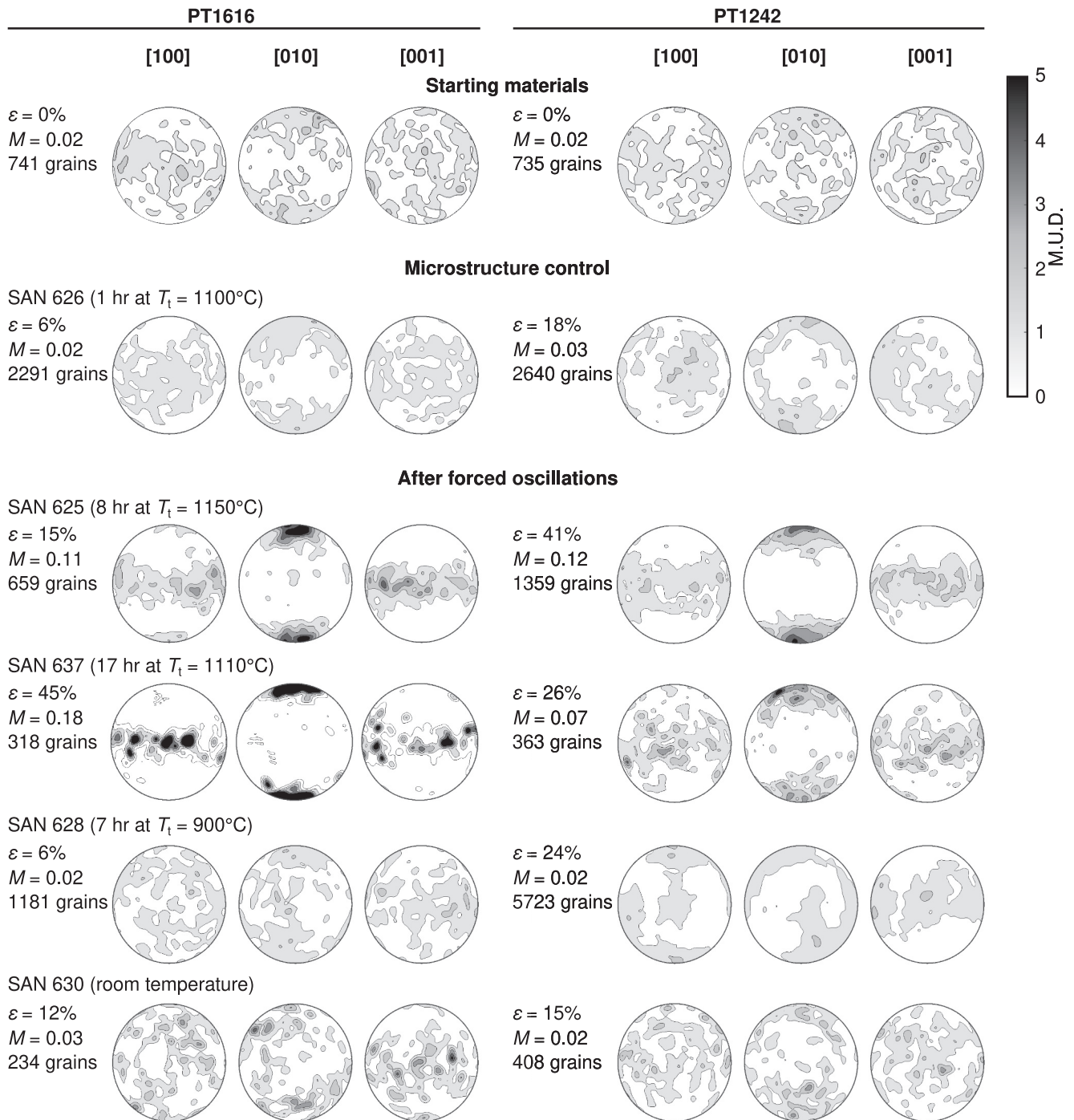


Figure 6. Selection of representative, lower-hemisphere, equal area, contour plots of crystallographic preferred orientation constructed from EBSD data using one point per grain. The final true strain, the M-index, and the number of grains are listed for each set of pole figures. The contour plots were produced using a halfwidth of 5° . The vertical direction is parallel to the compression direction for all pole figures. M.U.D. stands for multiples of uniform distribution.

heating stage. Therefore, there should be no significant change to furnace efficiency during each experiment. Nevertheless, due to run-to-run variability (i.e., furnace wall thickness, concentricity, etc.), the temperature uncertainty in high-temperature D-DIA experiments likely exceeds the $\pm 20^\circ\text{C}$ uncertainty associated with the temperature calibration alone. In the analysis that follows, we consider a temperature uncertainty of $\pm 50^\circ\text{C}$ among experiments, which is similar to the uncertainty reported for the temperature estimates based, alternatively, on the quartz-to-coesite transformation kinetics (Cross et al., 2025) and uncertainties reported in other D-

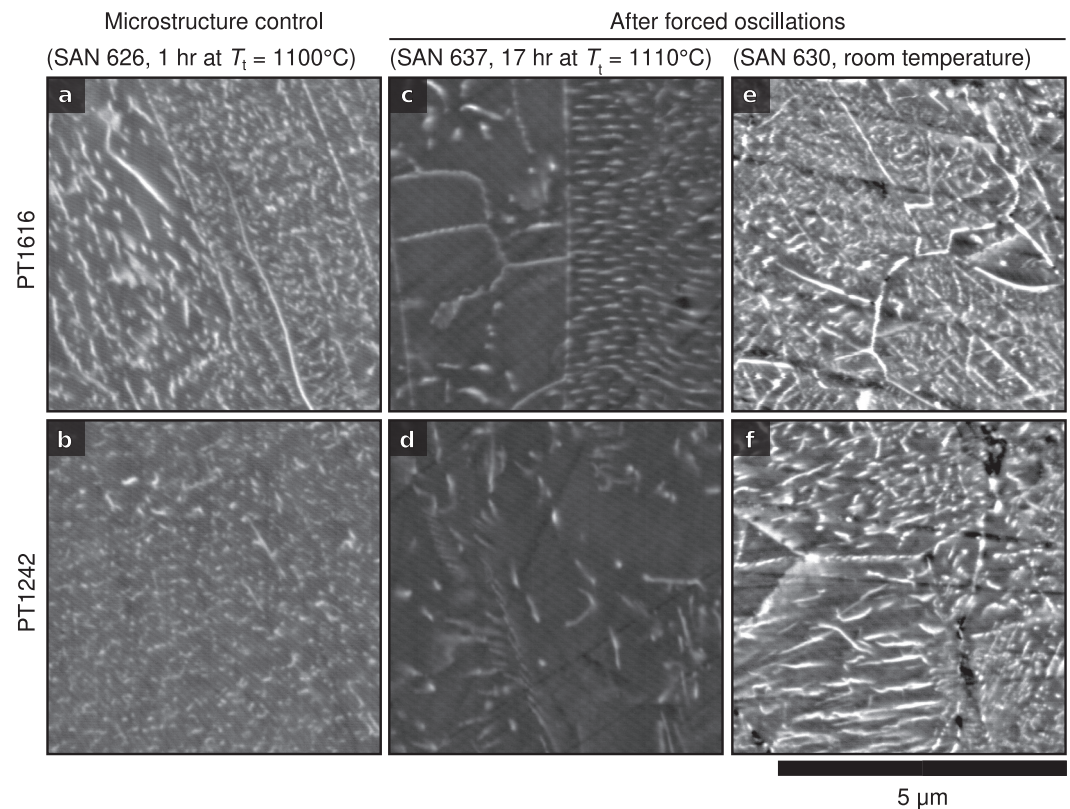


Figure 7. Representative backscatter-electron images of decorated dislocations in our samples. Bright spots and lines in these images are Fe-oxide precipitates along dislocation lines that intersect the sample surface. From left to right: microstructure-control experiment SAN 626, frequency-stepping experiment SAN 637, and room-temperature experiment SAN 630. Top and bottom rows present images of PT1616 and PT1242, respectively.

DIA studies (Dixon & Durham, 2018). Thankfully, temperature variability within an experiment does not suffer from the run-to-run variability of components in the assembly and is likely small (Dixon & Durham, 2018). Therefore, the observed frequency and amplitude dependencies presented in Figures 3 and 4 should be unaffected by temperature variability, as multiple frequencies and amplitudes were tested within a single experiment.

Changes in grain size throughout an experiment may also complicate the interpretation of our results. It is possible that grain-size sensitive mechanisms associated with grain-boundary sliding contributed to dissipation in our experiments (c.f. Faul & Jackson, 2015; Qu, 2022). Thus, a significant increase in grain size over the course of an experiment may impart a corresponding decrease in dissipation, and vice versa. Our microstructure-control experiment suggests that mean grain sizes of the top and bottom samples in our experiments stabilized to approximately 5 μm during the initial compression and relaxation. If so, then grain-size changes over the course of forced oscillations were less than one decade (Table 2) and likely had a negligible effect on viscoelastic behavior (c.f. Qu, 2022, Figure 5.10). Our high-temperature frequency-stepping experiment (SAN 637) supports this interpretation as mean grain sizes increased by a factor of three during forced oscillations, yet attenuation and modulus relaxation also increased from step 1 to step 5, which were both performed at a frequency of $10^{-2.48}$ Hz and similar amplitudes. This increase is opposite to what would be expected if grain-size sensitive dissipation mechanisms dominated the viscoelastic behavior of our samples. Therefore, we argue that grain-size evolution during forced oscillations had a negligible effect on the viscoelastic behavior.

The development of CPO in our samples could influence their nonlinear viscoelastic behavior through an increase in associated viscous anisotropy, thereby potentially skewing the observed correlations between Q^{-1} and E_{eff} and frequency or stress amplitude. In polycrystalline olivine under compression, CPO development produces hardening along the axial (compression) direction (Meyers & Kohlstedt, 2021). As such, the stress amplitudes required for amplitude-dependent attenuation may shift to progressively higher values relative to forced

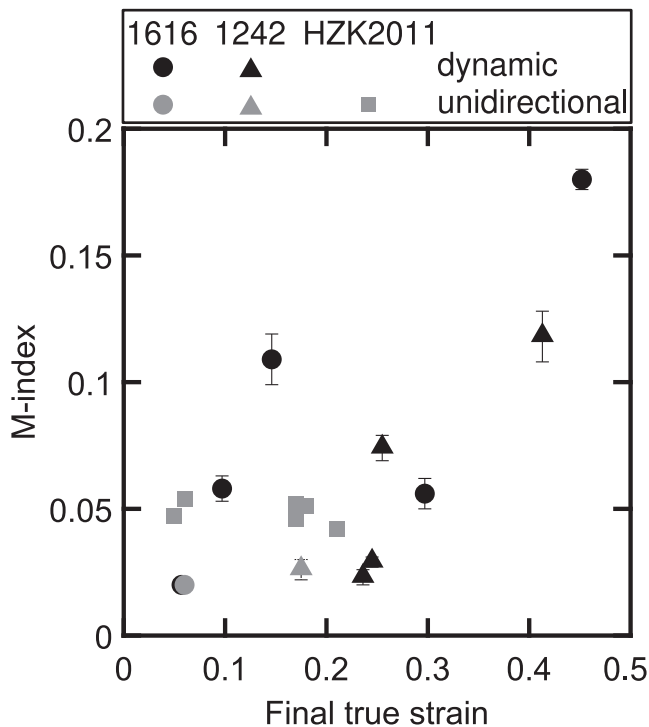


Figure 8. Crystallographic preferred orientation strength in polycrystalline San Carlos olivine as quantified by the M-index as a function of final strain for unidirectional (gray) and dynamic (black) axial deformation superposed on a unidirectional background deformation. PT1616 and PT1242 are indicated by circles and triangles, respectively. M-indices from Hansen et al. (2011) are plotted for comparison (squares). Error bars represent the standard deviation of the M-index as determined from 100 random samples of 300 grains.

oscillations on a randomly-textured aggregate. Hence, the development of a strong CPO should result in lower Q^{-1} values over time in axial forced-oscillation experiments. Figure 6 demonstrates that our samples from high-temperature experiments did develop a significant CPO, with M-indices up to 0.18. However, Q^{-1} consistently increases upon returning to previously imposed frequencies and similar amplitudes. We therefore infer that any effect of viscous anisotropy is at least obscured by the sensitivities of our samples to frequency and stress amplitude or other microstructural changes. Our observations agree with Hansen et al. (2012), who demonstrated that minimal viscous anisotropy is imparted by CPO with M-indices below 0.20. Therefore, we conclude that the development of viscous anisotropy did not significantly affect the viscoelastic behavior of our samples.

Interestingly, our results indicate that CPO development associated with unidirectional deformation is not affected by a superposed periodic deformation in our experiments. From a mechanical perspective, dynamic loading will cycle the CPO of a sample between that characteristic of shortening (i.e., resulting from axisymmetric triaxial compression) and that characteristic of extension (i.e., resulting from axisymmetric triaxial extension). As the shortening and extensional CPO types are similar in M-index and general shape (c.f. Hansen et al., 2011; Hansen et al., 2016), one might expect a stronger CPO to develop under dynamic loading than under unidirectional loading to the same final strain. Figure 8 presents a comparison of our results to M-indices obtained from unidirectional deformation experiments performed by Hansen et al. (2011) on San Carlos olivine in axial compression in a Paterson gas-medium apparatus at elevated temperatures and pressures. M-indices from our dynamically-deformed samples (Figure 8, black data) are similar to theirs at similar values of final strain. Therefore, for final shortening strains up to $\sim 20\%$ and strain amplitudes up to $\sim 2\%$ – 3% , there seems to be no significant effect of dynamic deformation on CPO evolution in our experiments.

Dislocation densities in our deformed samples indicate that the internal stresses in our samples remained relatively constant during forced oscillations. Figure 9 demonstrates that dislocation density correlates strongly with the flow stress of the initial compression. Importantly, the dislocation density of our microstructure-control experiment, which only underwent the initial compression and relaxation, is consistent with those of our dynamically loaded samples, indicating that the dislocation density, and hence the internal stress, remained relatively stable over the course of forced oscillations. Note that the slope of this correlation between dislocation density and stress in Figure 9 should not be compared to piezometric relationships for steady-state dislocation density as our dislocation densities were affected by the relaxation and forced oscillations following the initial compression.

Although noisier, another correlation exists between dislocation density and the maximum stress experienced during forced oscillations (Figure S2 in Supporting Information S1), which may explain the relatively elevated Q^{-1} upon stepping down in amplitude after forced oscillations at higher amplitudes (Figures S1 and S3 in Supporting Information S1). Even though the flow stress of the initial compression appears to have exerted a first-order control on the dislocation density, the high peak stresses during large-amplitude oscillations may have lead to subtle increases in dislocation density, which would result in minor increases in attenuation and modulus relaxation in subsequent forced oscillations at lower amplitudes. Such behavior is characteristic of dislocation damping (Gremaud, 2001, p. 179). Therefore, we suggest that Q^{-1} and E_{eff} from steps that decreased in amplitude may be influenced by stress history and are therefore less reliable than Q^{-1} and E_{eff} from steps that increased in amplitude. Nevertheless, further systematic investigation is required to confirm this effect of stress history on attenuation in olivine.

We conclude that any evolution of experimental conditions or microstructure over the course of our experiments did not significantly affect the viscoelastic behavior of our samples. Therefore, we argue that the results from our

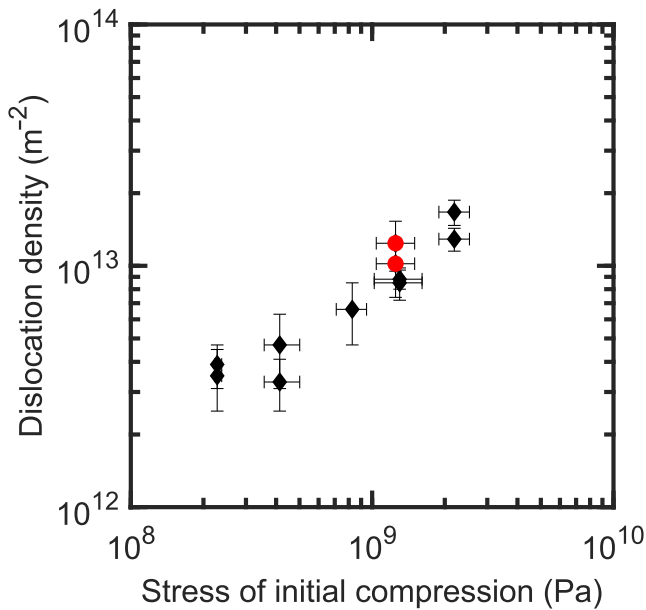


Figure 9. Dislocation density before (microstructure-control experiment, red circles) and after forced oscillations (black diamonds) and as a function of the average flow stress of the initial compression. Horizontal error bars represent the range of flow-stress estimates obtained from the (112), (131), and (130) lattice planes.

frequency-stepping experiments and the results from increasing-amplitude steps in our amplitude-stepping experiments are a suitable data set to compare to numerical solutions of the plastic-anisotropy and backstress models.

5.2. Comparison to Viscoelastic Models

Here we compare the results of our attenuation experiments to predictions of proposed models for the viscoelastic behavior of olivine. Figure 10 demonstrates that our samples exhibit much stronger attenuation ($Q^{-1} \sim 0.6$ – 10) than predicted by the recent, refined calibration of the extended Burgers model at similar conditions ($Q^{-1} \sim 0.003$ – 0.1) (Qu, 2022). This discrepancy corroborates our suggestion that additional dissipation mechanisms besides grain-boundary sliding and diffusion creep contributed to the viscoelastic behavior of our samples.

To compare the results of our forced-oscillation experiments to numerical solutions of the plastic-anisotropy and backstress models, we set temperatures, pressures, and stress amplitudes in the modeling to match the experiments. As previously discussed, we infer that the dislocation density remained constant, to first order, during forced oscillations. Therefore, we set up the numerical simulation with a constant bias stress that is reflective of the post-experiment dislocation densities in our samples following the piezometric relationship of Bai and Kohlstedt (1992). To model the frequency-stepping experiments, we apply a representative stress amplitude of 160 MPa. Furthermore, as experiment SAN 597 featured only one negligible step-increase in amplitude we choose to omit it from the comparison to the models.

Figure 10a reveals that both the backstress model (solid lines) and the plastic-anisotropy model (dotted lines) can produce strong attenuation and exhibit a Debye peak superposed on a Maxwell-type background dissipation, similar to the behavior of a Burgers model. Figure 10b illustrates that the plastic-anisotropy model produces a peak in $Q^{-1}(\sigma_A)$ superposed on a power-law slope with a stress exponent equal to $n - 1$. In contrast, the backstress model produces an exponential increase in Q^{-1} at high stress amplitudes, while a peak superposed on the nonlinear part of $Q^{-1}(\sigma_A)$ appears at lower temperatures, smaller bias stresses, shorter periods, or larger grain sizes.

Notably, both models tend toward linear behavior at low stress amplitudes (Figure 10b). The plastic-anisotropy model produces linear behavior when the stress amplitude is significantly smaller than the bias stress, whereas the backstress model produces linear behavior below a certain threshold amplitude. We hereafter refer to this threshold amplitude as the “threshold amplitude for nonlinearity,” which is dependent on temperature, grain size, and period, and is weakly dependent on bias stress. A detailed sensitivity analysis of both models is provided in Text S2 and Figures S5–S12 in Supporting Information S1.

The backstress model matches our data more closely than the plastic-anisotropy model. First, the observed frequency dependence of Q^{-1} and correlation of E_{eff} with frequency (Figures 3a–3e) in our experiments are consistent with the presence of a Debye peak centered around $\sim 10^{-3}$ Hz, superposed on Maxwell-type background dissipation. The backstress model features a Debye peak at similar frequencies, whereas the plastic-anisotropy model features a Debye peak at lower frequencies (Figure 10a). Second, the backstress model reasonably reproduces the amplitude-sensitivity of E_{eff} and Q^{-1} (Figures 10b and 10d). In general, the modulus relaxation (Figures 10c and 10d) is much better predicted by the backstress model. The plastic-anisotropy model can only be made to match the magnitude of Q^{-1} and E_{eff} in our experiments by multiplying the pre-exponents of the constitutive equations for creep of the soft and hard slip systems by factors of ~ 2 to $\sim 6 \times 10^3$ (see Text S2.1.1 in Supporting Information S1 for more details), which far exceed the uncertainty associated with these single-crystal flow laws for steady-state creep. We emphasize that our choice of bias stress or hard and soft slip systems for the plastic-anisotropy model does not significantly affect the conclusion of this comparison. We refer the reader to Text S2 and Figures S7, S8 in Supporting Information S1 for more details.

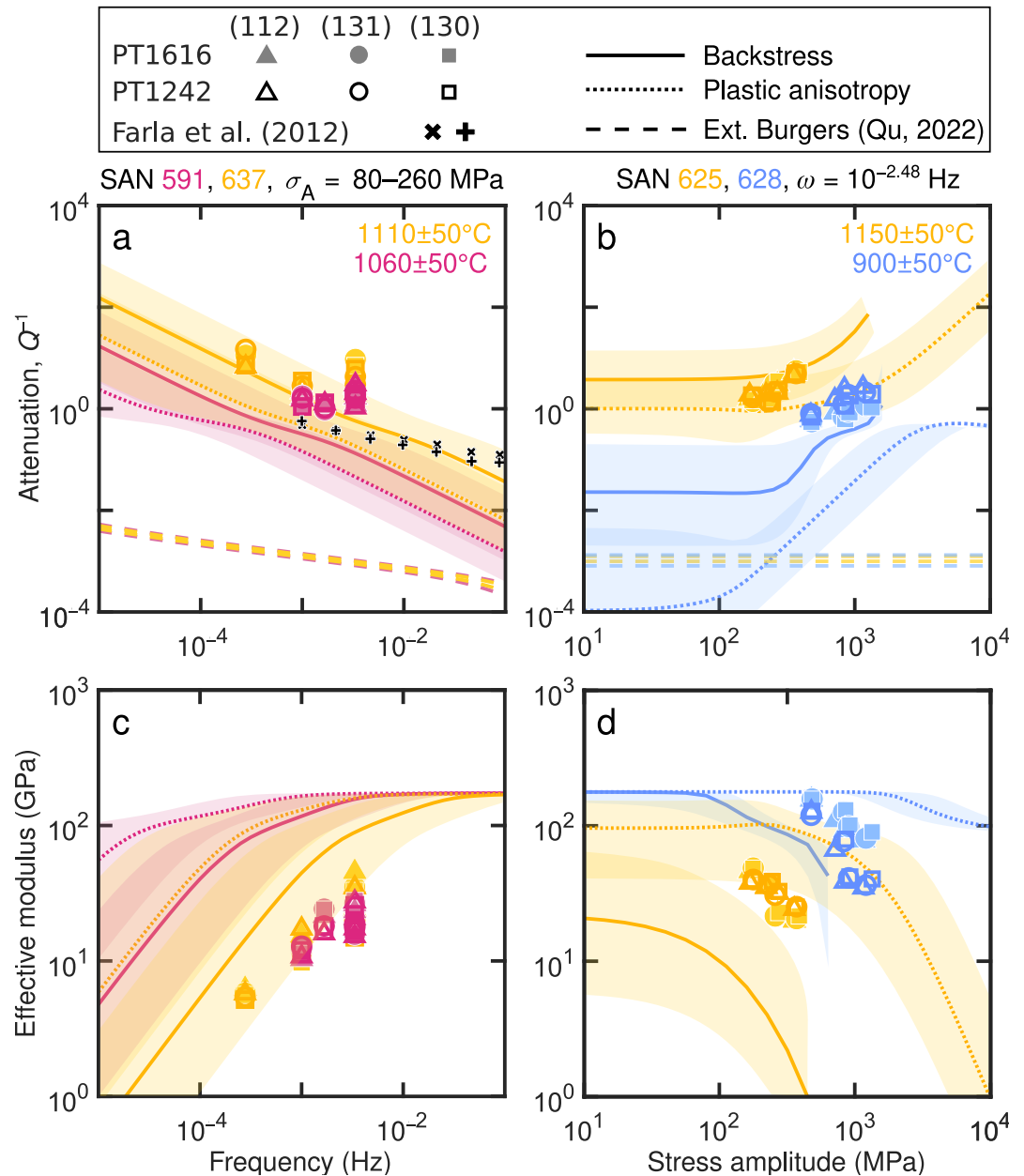


Figure 10. Comparison of viscoelastic behavior from experimental data (markers) to numerical solutions of the backstress model, plastic-anisotropy model, and extended Burgers model (solid, dotted, and dashed lines, respectively) as a function of frequency (panels a and c) and as a function of stress amplitude (panels b and d). Shaded areas represent the combined uncertainties in temperature and bias stress based on post-mortem dislocation density, and the range in post-mortem grain size. For our amplitude-stepping experiments, we only include steps of increasing stress amplitude to avoid any complicating effects of strain history, see text for discussion. Data from micro-strain torsional forced-oscillation experiments on predeformed polycrystalline olivine at 1100°C from Farla et al. (2012) are plotted in panel (a) with “+” and “x” symbols identifying prior deformation in compression and torsion, respectively. In panels (b, d), model lines truncate at the amplitude of numerical instability.

We also compared the intragranular plastic-anisotropy and backstress models to the results of micro-strain forced-oscillations on predeformed polycrystalline olivine by Farla et al. (2012). These experiments were performed at temperatures similar to our experiments, and their samples have similar post-mortem dislocation densities. They observed linear behavior over their range of shear-stress amplitudes (0.19–0.53 MPa) and a weak frequency dependence. Both the backstress model and the plastic-anisotropy model correctly predict such linear behavior at

these low amplitudes, but again, the magnitude of Q^{-1} predicted by the backstress model compares better to their observations (Figure 10a, “+” and “x” symbols) than the magnitude of Q^{-1} predicted by the plastic-anisotropy model. We note that the backstress model predicts a slightly stronger frequency dependence of attenuation than Farla et al. (2012) at high frequencies. In addition, the poor match of the backstress model with E_{eff} from our frequency-stepping experiment at 1060°C (SAN 591) and the viscoelastic behavior observed in our amplitude-stepping experiment at 900°C (SAN 628) illustrates the necessity of better temperature constraints in future experiments looking to test the nonlinear viscoelasticity of polycrystalline olivine.

Although the backstress model is able to predict the high-temperature behavior of polycrystalline olivine relatively well, it cannot explain the significant attenuation and consistent hysteresis with plastic-strain amplitudes on the order of $\sim 0.1\%$ – 0.5% that we observe at room temperature (Figure 4g). Therefore, other mechanisms may explain these observations, such as the microplastic mechanisms of geometrical-kink migration and isolated kink-pair nucleation and migration (Karato, 1998). The contribution of geometrical-kink migration to anelastic strain is small, following Equation 20 from Karato (1998), but significant anelastic strain may result from isolated kink-pair nucleation and migration. Karato (1998) describes the anelastic strain obtainable through isolated kink-pair nucleation and migration as $\epsilon_{\text{an,II}} = \Delta_{\text{II}} \epsilon_{\text{el,A}}$, in which $\epsilon_{\text{el,A}} = \sigma_{\text{A}}/E$ is the elastic strain at peak stress, σ_{A} , and Δ_{II} is the relaxation strength of kink-pair nucleation and migration, which is a function of dislocation density, ρ , pinning point spacing, L , and the angle that the geometrical kinks make to their Peierls potential valley, θ , as $\Delta_{\text{II}} = \rho L^2 \sin^2 \theta$. For a dislocation density of $\sim 10^{13} \text{ m}^{-2}$, an optimal orientation of $\theta = 45^\circ$, $\sigma_{\text{A}} \sim 1\text{--}3 \text{ GPa}$, and assuming that $L \sim \rho^{-1/2}$, the total anelastic microplastic strain would be on the order of 0.3% – 0.7% . Therefore, the anelastic strains observed in our room-temperature experiment are at least consistent with the anelastic strains predicted from these kink-based models.

5.3. Linearized Backstress Model

Most modeling applications of the viscoelastic behavior of the mantle require linear constitutive equations to remain computationally feasible. Fortunately, the backstress model, and more specifically its hyperbolic sine term (Equation 11), behaves linearly at low stress amplitudes. Additionally, at frequencies high enough to limit the amount of recovery in any given force oscillation, the recovery terms in Equation 12 may be neglected. This simplified model then behaves equivalent to a standard linear solid and produces linear anelastic behavior. The strain rate and Taylor-stress rate can then be expressed as

$$\dot{\epsilon}_{\text{p}} = A'(T) \sigma_{\rho}^2 \frac{\sigma - \sigma_{\text{b}}}{\sigma_{\text{ref}}(T)} \quad (14)$$

and

$$\dot{\sigma}_{\rho} = M \frac{\sigma_{\rho} + \sigma_{\text{d}}}{\sigma_{\rho}} \dot{\epsilon}_{\text{p}}, \quad (15)$$

respectively. Using these expressions, we derive a linear viscosity for dislocation glide,

$$\eta_1 = \frac{\sigma_{\text{ref}}(T)}{A'(T) \sigma_{\rho}^2}, \quad (16)$$

and a restoring modulus,

$$E_{\text{R}} = M \frac{\sigma_{\rho} + \sigma_{\text{d}}}{\sigma_{\rho}}, \quad (17)$$

This linear viscosity and restoring modulus can be used to define the complex modulus and its associated Q^{-1} as

$$E^*(\omega) = \left((E_{\text{R}} + \eta_1 \omega i)^{-1} + E_{\text{U}}^{-1} \right)^{-1}, \quad (18)$$

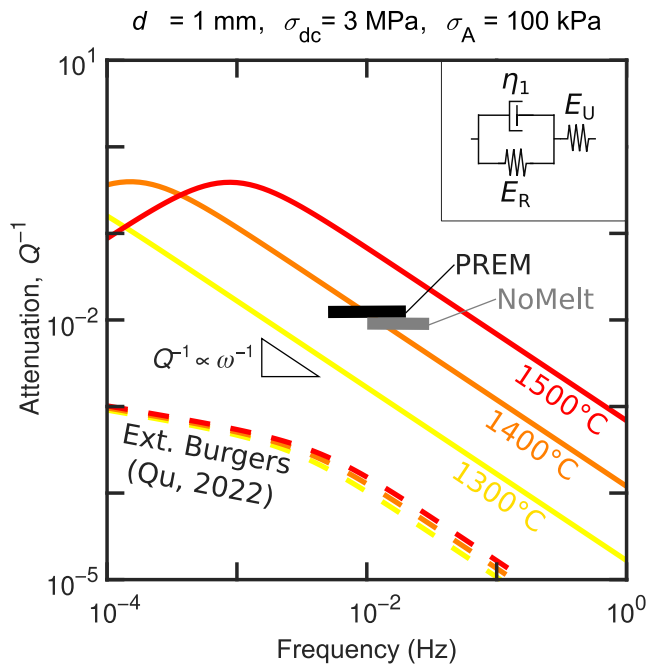


Figure 11. Attenuation as a function of frequency predicted by the linearized backstress (solid lines) and extended Burgers (dashed lines) models at conditions typical of seismic wave propagation in the upper-mantle. Black solid lines represent PREM and NoMelt attenuation models (based on geophysical measurements) at 120 km depth from Ma et al. (2020). The inset in the top right corner illustrates the spring and dashpot representation of the linearized backstress model.

and

$$Q^{-1}(\omega) = \frac{\eta_1 E_U \omega}{E_R^2 + E_R E_U + \eta_1^2 \omega^2}, \quad (19)$$

respectively. In Equation 18, E^* is the frequency-dependent complex modulus, and i is the imaginary unit. A spring and dashpot representation of the linearized backstress model is included in an inset in Figure 11.

This linearized version of the backstress model can reproduce the anelastic part of the full, nonlinear model given a suitably chosen Taylor stress, σ_p . Preliminary numerical investigation of Equations 14 and 15 indicates that σ_p is relatively insensitive to temperature (see Figure S13 in Supporting Information S1). Furthermore, assuming that σ_p equals the steady-state Taylor stress leads to an underestimation of the Maxwell frequency of the Debye peak.

5.4. Extrapolation to Upper-Mantle Conditions

As an illustrative example, we extrapolate the linearized backstress model to conditions relevant to seismic-wave attenuation in the upper mantle. Microstructural evidence of exhumed mantle rocks confirms that backstresses among dislocations play an important role at upper mantle conditions (Wallis et al., 2019, 2022). We assume a bias stress of 3 MPa based on a typical strain rate associated with mantle convection of $\sim 10^{-15} \text{ s}^{-1}$ and a typical long-term mantle viscosity $\sim 3 \times 10^{21} \text{ Pas}$ (the Haskell value Mitrova, 1996). We note that this bias stress likely represents an upper bound estimate for the bias stress in the asthenosphere and discuss the sensitivity of the predictions to lower bias stresses below. We further assume a grain size of 1 mm (Chatzaras et al., 2016), temperatures of 1400–1600°C (Ma et al., 2020), a pressure of

5 GPa, and a stress amplitude of 100 kPa, corresponding to typical seismic-wave strain amplitudes of $\sim 10^{-6}$ (Miyazawa et al., 2021). We find that taking a value for σ_p of 80% of the bias stress reasonably reproduces the full nonlinear model (Figure S13 in Supporting Information S1). Figure 11 compares the extrapolation of the linearized backstress model to the PREM and NoMelt attenuation models (Durek & Ekström, 1996; Ma et al., 2020) and the recent calibration of the extended Burgers model (Qu, 2022).

Figure 11 demonstrates that the backstress model is able to capture the magnitude of Rayleigh-wave attenuation at reasonable temperatures for the oceanic asthenosphere. Note that the backstress model is insensitive to stress amplitude under these conditions, and hence the choice of stress amplitude does not significantly influence the match of the backstress model to the attenuation models. In contrast, bias stress magnitude does have a significant effect. For example, a smaller bias stress of 1 MPa at otherwise the same conditions would lead to an underestimation of the attenuation in the asthenosphere by roughly one order of magnitude for a temperature of 1400°C. This result indicates that the ambient stress level, or more specifically the existing dislocation density, in the upper mantle may be an important variable to consider when interpreting thermomechanical conditions from seismic data.

As noted by Qu (2022), the recent calibration of the extended Burgers model underestimates the magnitude of attenuation in the upper mantle. Qu's updated calibration, based on forced-oscillation tests to larger grain sizes than previously explored, features a stronger grain-size sensitivity than the calibration of Jackson and Faul (2010). This increased grain-size sensitivity results in decreased Q^{-1} relative to the calibration of Jackson and Faul (2010) at the large grain sizes of olivine in the mantle.

Unfortunately, neither the backstress model nor the extended Burgers model currently reproduce the weak frequency dependence (i.e., dissipation band) of seismic-wave attenuation across the relevant frequency range, suggesting that either the models require modification or alternative mechanisms need to be invoked. One option

is the incorporation of a distribution of anelastic elements in the backstress model. A microphysical basis for this modification may be the distribution of length scales over which long-range dislocation interactions act within grains. These length scales may be tied to distributed (sub)grain size or internal stress heterogeneity. Alternatively, mechanisms that involve (pre-)melting (Faul et al., 2004; Yamauchi & Takei, 2024) or water (Liu et al., 2023) could help explain the weak frequency dependence of seismic-wave attenuation in the upper mantle. The effects of (pre-)melting and water on the amplitude-dependent viscoelastic behavior of polycrystalline olivine remain to be tested.

Observations of amplitude-dependent seismic-wave attenuation in the upper mantle underneath northeastern Japan by Tero and Nakajima (2024); Tero and Nakajima (2025) suggest a potential role of dislocations in the attenuation of seismic waves in the mantle wedge corner, raising the question whether the backstress mechanism may play a role in explaining their results. The average estimated stress drop associated with the earthquakes considered in these studies is on the order of 10 MPa, which is near the threshold amplitude for nonlinearity of the backstress model. Therefore, we speculate that the backstress model may have contributed to the nonlinear viscoelasticity inferred by these studies in the immediate vicinity of the Earthquake where stress amplitudes are largest. Further research is required to assess whether additional factors such as intracrystalline water or partial melting may lower the threshold amplitude for nonlinearity. Other potential causes of nonlinear viscoelastic behavior in the mantle wedge corner may include the intrinsic attenuation in partially serpentinized or otherwise microfractured rocks.

Acknowledgments

The authors like to thank I. Jackson and an anonymous reviewer for thorough and helpful formal reviews that improved this manuscript. The authors thank Amanda Dillman for technical assistance with synthesis of the starting materials and the dislocation decoration analysis. This research was performed on APS beam time award(s) (<https://doi.org/10.46936/APS-180066/60009559> and <https://doi.org/10.46936/APS-184759/60012253>) from the Advanced Photon Source, a U.S. Department of Energy Office of Science user facility operated for the Department of Energy Office of Science by Argonne National Laboratory under Contract No. DE-AC02-06CH11357. Use of the 6-BM-B beamline was supported by COMPRES, the Consortium for Materials Properties Research in Earth Sciences, under NSF Cooperative Agreement EAR-1661511. This work was supported by National Science Foundation (NSF) awards EAR-2218305 (to L.N.H.), EAR-2022433 (to L.N.H.), EAR-2023061 (to L.N.H.), EAR-1806791 (to K.M.K.), and EAR-2023128 (to A.J.C.). T.B. was supported by a fellowship from the Royal Commission for the Exhibition of 1851 and UKRI Grant MR/V021788/1. L.N.H. and T.B. were supported by NWO Grant ENW. GO.001.005. Parts of this work were carried out in the Characterization Facility, University of Minnesota, which receives partial support from the NSF through the MRSEC (Award Number DMR-2011401) and the NNCI (Award Number ECCS-2025124) programs. D.H. acknowledges support from Nick Seaton during the acquisition of the electron-backscatter diffraction data. Portions of this work were performed under the auspices of the U.S. Department of Energy by Lawrence Livermore National Laboratory under Contract DE-AC52-07NA27344. LLNL-JRNL-2000685.

6. Conclusions

We present forced-oscillation experiments performed in a deformation-DIA that test the frequency- and amplitude-dependent viscoelastic response of dry, melt-free, polycrystalline olivine at conditions favorable for investigating dislocation-based dissipation mechanisms. We observe that attenuation and modulus relaxation depend on stress amplitude, indicating that the observed viscoelastic behavior must be linked to dislocation-based mechanisms.

Analysis of pre- and post-experimental microstructures indicates that grain size and CPO evolution did not produce or significantly skew the observed correlations between attenuation or modulus relaxation and stress amplitude. In addition, dislocation density remained relatively constant over the course of the experiments.

We compare our results to numerical solutions of two dislocation-based microphysical models that were recently proposed by Karato (2021) and Breithaupt et al. (2023). We find that our experimental results compare well to the backstress model of Breithaupt et al. (2023), suggesting that intragranular interactions among dislocations may explain the nonlinear viscoelastic behavior observed in our experiments.

When extrapolated to conditions typical of seismic-wave propagation in the asthenosphere, the backstress model can explain the magnitude of attenuation predicted by various attenuation models, whereas the recently refined calibration of the extended Burgers model cannot. However, the incorporation of a distribution of anelastic elements into the backstress model or invoking mechanisms that involve premelting or water is necessary to account for the weak frequency dependence of attenuation in the upper mantle.

Currently, the backstress model is able to explain important aspects of viscoelastic behavior of polycrystalline olivine in seismic-wave attenuation (this study), and postseismic creep (Breithaupt et al., 2023). Therefore, intragranular dislocation interactions may control the transient rheological behavior of the upper mantle in a variety of Earth processes. Targets for future investigation include the applicability of the backstress model to GIA, normal mode attenuation, and solid-body tides of Earth and other planetary bodies.

Data Availability Statement

All data used in this study are available from the University of Minnesota Digital Conservancy (Hein et al., 2025).

References

- Abramson, E. H., Brown, J. M., Slutsky, L. J., & Zaug, J. (1997). The elastic constants of San Carlos olivine to 17 GPa. *Journal of Geophysical Research: Solid Earth*, 102(B6), 12253–12263. <https://doi.org/10.1029/97JB00682>
- Anderson, D. L., & Minster, J. B. (1979). The frequency dependence of Q in the Earth and implications for mantle rheology and Chandler wobble. *Geophysical Journal International*, 58(2), 431–440. <https://doi.org/10.1111/j.1365-246X.1979.tb01033.x>

- Ashby, M. F., & Duval, P. (1985). The creep of polycrystalline ice. *Cold Regions Science and Technology*, 11(3), 285–300. [https://doi.org/10.1016/0165-232X\(85\)90052-7](https://doi.org/10.1016/0165-232X(85)90052-7)
- Bachmann, F., Hielscher, R., & Schaeben, H. (2010). Texture analysis with MTEX – Free and open source software toolbox. *Solid State Phenomena*, 160, 63–68. <https://doi.org/10.4028/www.scientific.net/SSP.160.63>
- Bai, Q., & Kohlstedt, D. L. (1992). High-temperature creep of olivine single crystals, 2. Dislocation structures. *Tectonophysics*, 206(1), 1–29. [https://doi.org/10.1016/0040-1951\(92\)90365-D](https://doi.org/10.1016/0040-1951(92)90365-D)
- Bai, Q., Mackwell, S. J., & Kohlstedt, D. L. (1991). High-temperature creep of olivine single crystals 1. Mechanical results for buffered samples. *Journal of Geophysical Research: Solid Earth*, 96(B2), 2441–2463. <https://doi.org/10.1029/90JB01723>
- Billings, K., & Skemer, P. (2024). Evolving microstructure during experimental deformation of Maryland diabase. *Earth and Planetary Science Letters*, 627, 118564. <https://doi.org/10.1016/j.epsl.2023.118564>
- Boulze, H., Fleitout, L., Klein, E., & Vigny, C. (2022). Post-seismic motion after 3 Chilean megathrust earthquakes: A clue for a linear asthenospheric viscosity. *Geophysical Journal International*, 231(3), 1471–1478. <https://doi.org/10.1093/gji/ggac255>
- Breithaupt, T., Katz, R. F., Hansen, L. N., & Kumamoto, K. M. (2023). Dislocation theory of steady and transient creep of crystalline solids: Predictions for olivine. *Proceedings of the National Academy of Sciences*, 120(8), e2203448120. <https://doi.org/10.1073/pnas.2203448120>
- Camarano, F., & Romanowicz, B. (2008). Radial profiles of seismic attenuation in the upper mantle based on physical models. *Geophysical Journal International*, 175(1), 116–134. <https://doi.org/10.1111/j.1365-246X.2008.03863.x>
- Caron, L., Métivier, L., Greff-Lefftz, M., Fleitout, L., & Rouby, H. (2017). Inverting Glacial Isostatic Adjustment signal using Bayesian framework and two linearly relaxing rheologies. *Geophysical Journal International*, 209(2), 1126–1147. <https://doi.org/10.1093/gji/ggx083>
- Chatzaras, V., Kruckenberg, S. C., Cohen, S. M., Medaris, L. G., Jr., Withers, A. C., & Bagley, B. (2016). Axial-type olivine crystallographic preferred orientations: The effect of strain geometry on mantle texture. *Journal of Geophysical Research: Solid Earth*, 121(7), 4895–4922. <https://doi.org/10.1002/2015JB012628>
- Cooper, R. F. (2002). Seismic wave attenuation: Energy dissipation in viscoelastic crystalline solids. *Reviews in Mineralogy and Geochemistry*, 51(1), 253–290. <https://doi.org/10.2138/gsrmg.51.1.253>
- Cooper, R. F., Stone, D. S., & Ploekphol, T. (2016). Load relaxation of olivine single crystals. *Journal of Geophysical Research: Solid Earth*, 121(10), 7193–7210. <https://doi.org/10.1002/2016JB013425>
- Cross, A. J., Goddard, R. M., Kumamoto, K. M., Goldsby, D. L., Hansen, L. N., Chen, H., et al. (2025). Direct observations of transient weakening during phase transformations in quartz and olivine. *Nature Geoscience*, 18(6), 548–554. <https://doi.org/10.1038/s41561-025-01703-6>
- Dixon, N. A., & Durham, W. B. (2018). Measurement of activation volume for creep of dry olivine at upper-mantle conditions. *Journal of Geophysical Research: Solid Earth*, 123(10), 8459–8473. <https://doi.org/10.1029/2018JB015853>
- Doin, M.-P., Fleitout, L., & Christensen, U. (1997). Mantle convection and stability of depleted and undepleted continental lithosphere. *Journal of Geophysical Research: Solid Earth*, 102(B2), 2771–2787. <https://doi.org/10.1029/96JB03271>
- Durek, J. J., & Ekström, G. (1996). A radial model of anelasticity consistent with long-period surface-wave attenuation. *Bulletin of the Seismological Society of America*, 86(1A), 144–158. <https://doi.org/10.1785/BSSA08601A0144>
- Farla, R. J. M., Jackson, I., Fitz Gerald, J. D., Faul, U. H., & Zimmerman, M. E. (2012). Dislocation damping and anisotropic seismic wave attenuation in Earth's upper mantle. *Science*, 336(6079), 332–335. <https://doi.org/10.1126/science.1218318>
- Faul, U., Fitz Gerald, J. D., & Jackson, I. (2004). Shear wave attenuation and dispersion in melt-bearing olivine polycrystals: 2. Microstructural interpretation and seismological implications. *Journal of Geophysical Research: Solid Earth*, 109(B6). <https://doi.org/10.1029/2003JB002407>
- Faul, U., & Jackson, I. (2015). Transient creep and strain energy dissipation: An experimental perspective. *Annual Review of Earth and Planetary Sciences*, 43(1), 541–569. <https://doi.org/10.1146/annurev-earth-060313-054732>
- Freed, A. M., Hirth, G., & Behn, M. D. (2012). Using short-term postseismic displacements to infer the ambient deformation conditions of the upper mantle. *Journal of Geophysical Research: Solid Earth*, 117(B1). <https://doi.org/10.1029/2011JB008562>
- Goddard, R. M., Hansen, L. N., Wallis, D., Stipp, M., Holyoke III, C. W., Kumamoto, K. M., & Kohlstedt, D. L. (2020). A subgrain-size piezometer calibrated for EBSD. *Geophysical Research Letters*, 47(23), e2020GL090056. <https://doi.org/10.1029/2020GL090056>
- Goddard, R. M., Kumamoto, K., Hansen, L., Wallis, D., Cross, A. J., & Thom, C. A. (2023). Validation of subgrain-size piezometry as a tool for measuring stress in polymineralic rocks (preprint). *Preprints*. <https://doi.org/10.22541/essoar.169755254.46171679/v1>
- Gremaud, G. (2001). 3.3 dislocation - Point defect interactions. *Materials Science Forum*, 366–368, 178–246. <https://doi.org/10.4028/www.scientific.net/MSF.366-368.178>
- Gribb, T. T., & Cooper, R. F. (1998). Low-frequency shear attenuation in polycrystalline olivine: Grain boundary diffusion and the physical significance of the Andrade model for viscoelastic rheology. *Journal of Geophysical Research: Solid Earth*, 103(B11), 27267–27279. <https://doi.org/10.1029/98JB02786>
- Gueguen, Y., Darot, M., Mazot, P., & Woignard, J. (1989). Q1 of forsterite single crystals. *Physics of the Earth and Planetary Interiors*, 55(3), 254–258. [https://doi.org/10.1016/0031-9201\(89\)90073-3](https://doi.org/10.1016/0031-9201(89)90073-3)
- Hansen, L. N., Kumamoto, K. M., Thom, C. A., Wallis, D., Durham, W. B., Goldsby, D. L., et al. (2019). Low-temperature plasticity in olivine: Grain size, strain hardening, and the strength of the lithosphere. *Journal of Geophysical Research: Solid Earth*, 124(6), 5427–5449. <https://doi.org/10.1029/2018JB016736>
- Hansen, L. N., Wallis, D., Breithaupt, T., Thom, C. A., & Kempton, I. (2021). Dislocation creep of olivine: Backstress evolution controls transient creep at high temperatures. *Journal of Geophysical Research: Solid Earth*, 126(5), e2020JB021325. <https://doi.org/10.1029/2020JB021325>
- Hansen, L. N., Warren, J. M., Zimmerman, M. E., & Kohlstedt, D. L. (2016). Viscous anisotropy of textured olivine aggregates, Part 1: Measurement of the magnitude and evolution of anisotropy. *Earth and Planetary Science Letters*, 445, 92–103. <https://doi.org/10.1016/j.epsl.2016.04.008>
- Hansen, L. N., Zimmerman, M. E., & Kohlstedt, D. L. (2011). Grain boundary sliding in San Carlos olivine: Flow law parameters and crystallographic-preferred orientation. *Journal of Geophysical Research: Solid Earth*, 116(B8), B08201. <https://doi.org/10.1029/2011JB008220>
- Hansen, L. N., Zimmerman, M. E., & Kohlstedt, D. L. (2012). Laboratory measurements of the viscous anisotropy of olivine aggregates. *Nature*, 492(7429), 415–418. <https://doi.org/10.1038/nature11671>
- Hanson, D. R., & Spetzler, H. A. (1994). Transient creep in natural and synthetic, iron-bearing olivine single crystals: Mechanical results and dislocation microstructures. *Tectonophysics*, 235(4), 293–315. [https://doi.org/10.1016/0040-1951\(94\)90191-0](https://doi.org/10.1016/0040-1951(94)90191-0)
- Hein, D., Hansen, L. N., Kumamoto, K., Chen, H., Nehring, A., Goddard, R., et al. (2025). Data associated with Forced oscillation D-DIA experiments testing the nonlinear viscosity of the upper mantle [Dataset]. *DRUM*. <https://doi.org/10.13020/bec5-7533>
- Holtzman, B. K., Chrysoschoos, A., & Daridon, L. (2018). A thermomechanical framework for analysis of microstructural evolution: Application to olivine rocks at high temperature. *Journal of Geophysical Research: Solid Earth*, 123(10), 8474–8507. <https://doi.org/10.1029/2018JB015613>

- Huebner, J. S., & Sato, M. (1970). The oxygen fugacity-temperature relationships of manganese oxide and nickel oxide buffers. *American Mineralogist*, 55(5–6), 934–952.
- Isaak, D. G. (1992). High-temperature elasticity of iron-bearing olivines. *Journal of Geophysical Research: Solid Earth*, 97(B2), 1871–1885. <https://doi.org/10.1029/91JB02675>
- Jackson, I., & Faul, U. H. (2010). Grain-size-sensitive viscoelastic relaxation in olivine: Towards a robust laboratory-based model for seismological application. *Physics of the Earth and Planetary Interiors*, 183(1), 151–163. <https://doi.org/10.1016/j.pepi.2010.09.005>
- Karato, S. (1987). Scanning electron microscope observation of dislocations in olivine. *Physics and Chemistry of Minerals*, 14(3), 245–248. <https://doi.org/10.1007/BF00307989>
- Karato, S. (1998). A dislocation model of seismic wave attenuation and micro-creep in the Earth: Harold Jeffreys and the rheology of the solid Earth. *Pure and Applied Geophysics*, 153(2), 239–256. <https://doi.org/10.1007/s000240050195>
- Karato, S. (2021). A theory of inter-granular transient dislocation creep: Implications for the geophysical studies on mantle rheology. *Journal of Geophysical Research: Solid Earth*, 126(10), e2021JB022763. <https://doi.org/10.1029/2021JB022763>
- Karato, S., & Spetzler, H. A. (1990). Defect microdynamics in minerals and solid-state mechanisms of seismic wave attenuation and velocity dispersion in the mantle. *Reviews of Geophysics*, 28(4), 399–421. <https://doi.org/10.1029/RG028i004p00399>
- Klein, E., Fleitout, L., Vigny, C., & Garaud, J. (2016). Afterslip and viscoelastic relaxation model inferred from the large-scale post-seismic deformation following the 2010 Mw 8.8 Maule earthquake (Chile). *Geophysical Journal International*, 205(3), 1455–1472. <https://doi.org/10.1093/gji/ggw086>
- Kohlstedt, D. L., Goetze, C., Durham, W. B., & Vander Sande, J. (1976). New technique for decorating dislocations in olivine. *Science*, 191(4231), 1045–1046. <https://doi.org/10.1126/science.191.4231.1045>
- Lakes, R. S. (2009). *Viscoelastic materials*. Cambridge University Press. (Google-Books-ID: BH6f2hWWBkAC).
- Lau, H. C. P., & Holtzman, B. K. (2019). “Measures of dissipation in viscoelastic media” extended: Toward continuous characterization across very broad geophysical time scales. *Geophysical Research Letters*, 46(16), 9544–9553. <https://doi.org/10.1029/2019GL083529>
- Lau, H. C. P., Mitrovica, J. X., Auermann, J., Crawford, O., Al-Attar, D., & Latychev, K. (2016). Inferences of mantle viscosity based on ice age data sets: Radial structure. *Journal of Geophysical Research: Solid Earth*, 121(10), 6991–7012. <https://doi.org/10.1002/2016JB013043>
- Lekić, V., Matas, J., Panning, M., & Romanowicz, B. (2009). Measurement and implications of frequency dependence of attenuation. *Earth and Planetary Science Letters*, 282(1), 285–293. <https://doi.org/10.1016/j.epsl.2009.03.030>
- Li, L., & Weidner, D. J. (2007). Energy dissipation of materials at high pressure and high temperature. *Review of Scientific Instruments*, 78(5), 053902. <https://doi.org/10.1063/1.2735587>
- Li, L., & Weidner, D. J. (2010). Note: Synchronized stress-strain measurements in dynamic loading at high pressure using D-DIA. *Review of Scientific Instruments*, 81(9), 096102. <https://doi.org/10.1063/1.3481163>
- Liu, C., Yoshino, T., Yamazaki, D., Tsujino, N., Gomi, H., Sakurai, M., et al. (2023). Effect of water on seismic attenuation of the upper mantle: The origin of the sharp lithosphere–asthenosphere boundary. *Proceedings of the National Academy of Sciences*, 120(32), e2221770120. <https://doi.org/10.1073/pnas.2221770120>
- Ma, Z., Dalton, C. A., Russell, J. B., Gaherty, J. B., Hirth, G., & Forsyth, D. W. (2020). Shear attenuation and anelastic mechanisms in the central Pacific upper mantle. *Earth and Planetary Science Letters*, 536, 116148. <https://doi.org/10.1016/j.epsl.2020.116148>
- Masuti, S., & Barbot, S. (2021). MCMC inversion of the transient and steady-state creep flow law parameters of dunite under dry and wet conditions. *Earth Planets and Space*, 73(1), 208. <https://doi.org/10.1186/s40623-021-01543-9>
- McCarthy, C., Takei, Y., & Hiraga, T. (2011). Experimental study of attenuation and dispersion over a broad frequency range: 2. The universal scaling of polycrystalline materials. *Journal of Geophysical Research: Solid Earth*, 116(B9), B09207. <https://doi.org/10.1029/2011JB008384>
- Mei, S., Kohlstedt, D. L., Durham, W. B., & Wang, L. (2008). Experimental investigation of the creep behavior of MgO at high pressures. *Physics of the Earth and Planetary Interiors*, 170(3), 170–175. <https://doi.org/10.1016/j.pepi.2008.06.030>
- Meyers, C. D., & Kohlstedt, D. L. (2021). Experimental measurements of anisotropic viscosity in naturally sourced dunite with a preexisting CPO. *Tectonophysics*, 815, 228949. <https://doi.org/10.1016/j.tecto.2021.228949>
- Mitrovica, J. X. (1996). Haskell [1935] revisited. *Journal of Geophysical Research: Solid Earth*, 101(B1), 555–569. <https://doi.org/10.1029/95JB03208>
- Miyazawa, M., Brodsky, E. E., & Guo, H. (2021). Dynamic earthquake triggering in southern California in high resolution: Intensity, time decay, and regional variability. *AGU Advances*, 2(2), e2020AV000309. <https://doi.org/10.1029/2020AV000309>
- Morris, S. J. S., & Jackson, I. (2009). Diffusionally assisted grain-boundary sliding and viscoelasticity of polycrystals. *Journal of the Mechanics and Physics of Solids*, 57(4), 744–761. <https://doi.org/10.1016/j.jmps.2008.12.006>
- Mulyukova, E., & Bercovici, D. (2022). On the co-evolution of dislocations and grains in deforming rocks. *Physics of the Earth and Planetary Interiors*, 328, 106874. <https://doi.org/10.1016/j.pepi.2022.106874>
- Muto, J., Moore, J. D. P., Barbot, S., Iinuma, T., Ohta, Y., & Iwamori, H. (2019). Coupled afterslip and transient mantle flow after the 2011 Tohoku earthquake. *Science Advances*, 5(9), eaaw1164. <https://doi.org/10.1126/sciadv.aaw1164>
- Nield, G. A., Whitehouse, P. L., van der Wal, W., Blank, B., O'Donnell, J. P., & Stuart, G. W. (2018). The impact of lateral variations in lithospheric thickness on glacial isostatic adjustment in West Antarctica. *Geophysical Journal International*, 214(2), 811–824. <https://doi.org/10.1093/gji/ggy158>
- Nowick, A. S., & Berry, B. S. (1972). *Anelastic relaxation in crystalline solids*. Academic Press.
- Paterson, M. (1990). Rock deformation experimentation. In *The brittle-ductile transition in rocks* (Vol. 56, pp. 187–194). American Geophysical Union. <https://doi.org/10.1029/GM056p0187>
- Pollitz, F. F. (2003). Transient rheology of the uppermost mantle beneath the Mojave Desert, California. *Earth and Planetary Science Letters*, 215(1), 89–104. [https://doi.org/10.1016/S0012-821X\(03\)00432-1](https://doi.org/10.1016/S0012-821X(03)00432-1)
- Pollitz, F. F. (2005). Transient rheology of the upper mantle beneath central Alaska inferred from the crustal velocity field following the 2002 Denali earthquake. *Journal of Geophysical Research: Solid Earth*, 110(B8). <https://doi.org/10.1029/2005JB003672>
- Priestley, K., & McKenzie, D. (2013). The relationship between shear wave velocity, temperature, attenuation and viscosity in the shallow part of the mantle. *Earth and Planetary Science Letters*, 381, 78–91. <https://doi.org/10.1016/j.epsl.2013.08.022>
- Qausar, M. (1989). Attenuation properties of viscoelastic material. *Pure and Applied Geophysics*, 131(4), 703–713. <https://doi.org/10.1007/BF00876269>
- Qu, T. (2022). *Microstrain mechanical testing of ultramafic materials: The onset of anelastic relaxation, its grain-size sensitivity, and the role of orthopyroxene* (Thesis). Australian National University. Retrieved from <https://openresearch-repository.anu.edu.au/handle/1885/272419>
- Raterron, P., Merkel, S., & Holyoke, C. W., III. (2013). Axial temperature gradient and stress measurements in the deformation-DIA cell using alumina pistons. *Review of Scientific Instruments*, 84(4), 043906. <https://doi.org/10.1063/1.4801956>

- Sasaki, Y., Takei, Y., McCarthy, C., & Rudge, J. F. (2019). Experimental study of dislocation damping using a rock analogue. *Journal of Geophysical Research: Solid Earth*, 124(7), 6523–6541. <https://doi.org/10.1029/2018JB016906>
- Silber, R. E., Girard, J., & Karato, S.-I. (2022). Effects of pressure on diffusion creep in wet olivine aggregates. *Physics of the Earth and Planetary Interiors*, 324, 106840. <https://doi.org/10.1016/j.pepi.2022.106840>
- Skemer, P., Katayama, I., Jiang, Z., & Karato, S.-I. (2005). The misorientation index: Development of a new method for calculating the strength of lattice-preferred orientation. *Tectonophysics*, 411(1), 157–167. <https://doi.org/10.1016/j.tecto.2005.08.023>
- Takei, Y. (2022). Effect of impurities on polycrystal anelasticity. *Journal of Geophysical Research: Solid Earth*, 127(4), e2021JB023224. <https://doi.org/10.1029/2021JB023224>
- Tero, H., & Nakajima, J. (2024). Amplitude-dependent energy dissipation inferred from spectral analyses of intraslab earthquakes. *Journal of Geophysical Research: Solid Earth*, 129(5), e2023JB028492. <https://doi.org/10.1029/2023JB028492>
- Tero, H., & Nakajima, J. (2025). Seismological observations on amplitude-dependent energy dissipation in the crust and uppermost mantle. *Geophysical Research Letters*, 52(1), e2024GL112427. <https://doi.org/10.1029/2024GL112427>
- Underwood, E. (1970). *Quantitative stereology*. Addison-Wesley Publishing Company.
- Wallis, D., Hansen, L. N., Tasaka, M., Kumamoto, K. M., Parsons, A. J., Lloyd, G. E., et al. (2019). The impact of water on slip system activity in olivine and the formation of bimodal crystallographic preferred orientations. *Earth and Planetary Science Letters*, 508, 51–61. <https://doi.org/10.1016/j.epsl.2018.12.007>
- Wallis, D., Sep, M., & Hansen, L. N. (2022). Transient creep in subduction zones by long-range dislocation interactions in olivine. *Journal of Geophysical Research: Solid Earth*, 127(1), e2021JB022618. <https://doi.org/10.1029/2021JB022618>
- Wang, Y., Durham, W. B., Getting, I. C., & Weidner, D. J. (2003). The deformation-DIA: A new apparatus for high temperature triaxial deformation to pressures up to 15 GPa. *Review of Scientific Instruments*, 74(6), 3002–3011. <https://doi.org/10.1063/1.1570948>
- Weidner, D. J., Vaughan, M. T., Wang, L., Long, H., Li, L., Dixon, N. A., & Durham, W. B. (2010). Precise stress measurements with white synchrotron x rays. *Review of Scientific Instruments*, 81(1), 013903. <https://doi.org/10.1063/1.3263760>
- Weiss, J. R., Qiu, Q., Barbot, S., Wright, T. J., Foster, J. H., Saunders, A., et al. (2019). Illuminating subduction zone rheological properties in the wake of a giant earthquake. *Science Advances*, 5(12), eaax6720. <https://doi.org/10.1126/sciadv.aax6720>
- Yamauchi, H., & Takei, Y. (2016). Polycrystal anelasticity at near-solidus temperatures. *Journal of Geophysical Research: Solid Earth*, 121(11), 7790–7820. <https://doi.org/10.1002/2016JB013316>
- Yamauchi, H., & Takei, Y. (2024). Effect of melt on polycrystal anelasticity. *Journal of Geophysical Research: Solid Earth*, 129(4), e2023JB027738. <https://doi.org/10.1029/2023JB027738>
- Yuen, D. A., Sabadini, R. C. A., Gasperini, P., & Boschi, E. (1986). On transient rheology and glacial isostasy. *Journal of Geophysical Research: Solid Earth*, 91(B11), 11420–11438. <https://doi.org/10.1029/JB091iB11p11420>
- Zhong, S., Zuber, M. T., Moresi, L., & Gurnis, M. (2000). Role of temperature-dependent viscosity and surface plates in spherical shell models of mantle convection. *Journal of Geophysical Research: Solid Earth*, 105(B5), 11063–11082. <https://doi.org/10.1029/2000JB900003>